Journal of Materials Chemistry A

REVIEW

View Article Online
View Journal | View Issue

Cite this: J. Mater. Chem. A, 2019, 7, 5069

Recent advances in layered double hydroxide electrocatalysts for the oxygen evolution reaction

Zhengyang Cai,[a] Xiuming Bu,[b] Ping Wang, *[ac] Johnny C. Ho,[b] Junhe Yang[ac] and Xianying Wang*[ac]

Received 23rd November 2018
Accepted 25th January 2019

DOI: 10.1039/c8ta11273h

rsc.li/materials-a

The energy consumption of hydrogen production from electrolytic water splitting originates from the oxygen evolution reaction (OER). Development of efficient and cost-effective OER electrocatalysts has become a high-priority research task. In this regard, layered double hydroxides (LDHs) as one of the promising OER electrocatalysts have been intensely researched due to their unique 2D layered structure and excellent physicochemical properties. Herein, this review aims to summarize recent strategies to design LDHs, including nanostructuring, hybrid LDHs with conductive materials, partial substitution of cations, interlayer anion replacement, vacancy creation, and combination of computational methods and operando techniques. Specifically, a thorough literature overview in the developments of LDHs to improve OER performance is appraised in detail, based on the compositional difference of transition metal components. Challenges and future directions in designing LDHs as OER electrocatalysts are discussed. The provided discussion will be favorable to explore and develop better catalysts and device units for practical applications and will offer a basic understanding of the OER process along with key issues to evaluate the performance.

1. Introduction

As renewable energy sources continue the global success story, the demand for integrating them into the current energy and industry landscape grows. Hydrogen (H_2) is predicted to be a promising energy storage medium or carrier, with the advantages of high energy density (140 MJ kg^{-1}) which far exceeds those of gasoline and coal, environmental friendliness without carbon emission, and a useful by-product of water from combustion.[1,2] However, nearly 95% of H_2 is still produced from hydrocarbons, such as fossil fuels or biomass by reforming or thermal cracking which is severely restricted by its high air emission and high cost.[3–6] Water electrolysis is recognized to be one of the simplest methods for hydrogen production, namely electrochemically splitting water into hydrogen and oxygen.

[a]School of Materials Science and Technology, University of Shanghai for Science and Technology, Jungong Road 516, 200093 Shanghai, P. R. China. E-mail: ping.wang@usst.edu.cn; xianyingwang@usst.edu.cn
[b]Department of Materials Science and Engineering, City University of Hong Kong, 83 Tat Chee Avenue, Kowloon, Hong Kong, P. R. China
[c]Shanghai Innovation Institute for Materials, 200444 Shanghai, P. R. China

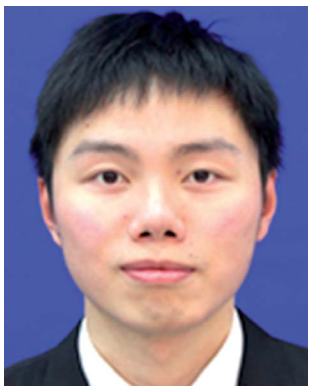

Mr Zhengyang Cai received his Bachelor's degree from the Nanjing Institute of Technology, P. R. China in 2017. Now he is pursuing his Master's degree under the supervision of Prof. Xianying Wang at the School of Materials Science and Engineering, University of Shanghai for Science and Technology, P. R. China. His current research interests include synthesis of electrocatalysts and their applications in electrocatalytic energy conversion.

Mr Xiuming Bu received his MS degrees from the School of Materials Science and Engineering, University of Shanghai for Science and Technology, P. R. China in 2017. Currently, he is a PhD student under the supervision of Professor Johnny C. Ho in the Department of Materials Science and Engineering at City University of Hong Kong. His research interests are the fabrication of nanomaterials and their applications in electronics and energy conversion.

This technology delivers "green" hydrogen with low cost and high efficiency. The only inputs needed are water and renewable electricity from wind, hydropower or photovoltaics.[7] Typically, a water electrolysis system is composed of a water electrolysis cell stack equipped with a cathode and an anode, at which the cathodic hydrogen evolution reaction (HER) and anodic oxygen evolution reaction (OER) occur, respectively (shown in Fig. 1). The OER involves a four-electron transfer and therefore the feasibility of the system as a sustainable hydrogen production technology ultimately depends on the sluggish OER. The reaction occurring under acidic and alkaline conditions is the most energy-demanding step during the whole water splitting process, as presented in eqn (1) and (2), respectively.[8,9]

$$2H_2O \rightarrow O_2 + 4H^+ + 4e^- \quad (1)$$

$$4OH^- \rightarrow O_2 + 2H_2O + 4e^- \quad (2)$$

Taking the significance and challenges of the OER into consideration, designing OER electrocatalysts is very crucial for renewable energy storage and conversion devices. Currently, the use of precious metals and precious metal-based oxides is drastically increasing, due to the benefit of excellent OER performance, especially Ru, Ir and their oxides.[10–17] However, it was extremely limited for potential application in a large scale because of their scarcity, high cost[16,18] and poor stability in strong alkaline solutions.[12,19–22] In parallel with these efforts on

Dr Ping Wang is currently an Associate Professor in the School of Materials Science & Engineering, University of Shanghai for Science and Technology, P. R. China. He obtained a bachelor's degree from the Hunan Institute of Science and Technology, P. R. China in 2007 and a Master's degree from East China Normal University, P. R. China in 2011. He then received his PhD degree from Ruhr-University Bochum, Germany in 2014 under the supervision of Prof. Dr. Michael Wark & Prof. Dr. Martin Muhler and worked as a postdoctoral fellow in the group of Prof. Dr. Jae Sung Lee at the Ulsan National Institute of Science and Technology, South Korea in 2015. His current research interests focus on the development of nanomaterials photo/electrocatalysts for water splitting and photo/electrocatalytic devices.

Prof Junhe Yang is currently a full professor in the School of Materials Science & Engineering, University of Shanghai for Science and Technology, P. R. China and vice dean of the Shanghai Institute of Materials Innovation, P. R. China. He received a PhD degree from Northeastern University, P. R. China in 2000. He visited the department of Mechanical Materials engineering in the University of Pittsburg, the United States as a visiting scholar from 2005 to 2006. His research interests center on graphene composites, carbon based porous functional materials, nano-carbon materials, special graphite materials, and coke quality control technology.

Prof Johnny C. Ho received his BS with high honors in Chemical Engineering in 2002 and his MS and PhD in Materials Science and Engineering from the University of California, Berkeley, in 2005 and 2009, respectively. From 2009 to 2010, he worked as a post-doctoral research fellow in the nanoscale synthesis and characterization group at Lawrence Livermore National Laboratory, California. Currently, he is an Associate Professor of Materials Science and Engineering at City University of Hong Kong. His research interests focus on the synthesis, characterization, integration and device applications of nanoscale materials for various technological applications, including nanoelectronics, sensors and energy harvesting.

Prof Xianying Wang is currently a full professor in the School of Materials Science & Engineering, University of Shanghai for Science and Technology, P. R. China. She received a PhD degree from the Shanghai Institute of Microsystems and Information Technology, Chinese Academy of Sciences, P. R. China in 2005. From 2007 to 2008, she visited the Lawrence Livermore National Laboratory, the United States, as a visiting scholar. Her research interests focuses on semiconductor nanomaterials and their applications spanning from photo/electro/mechanical energy conversion to sensor and other related fields.

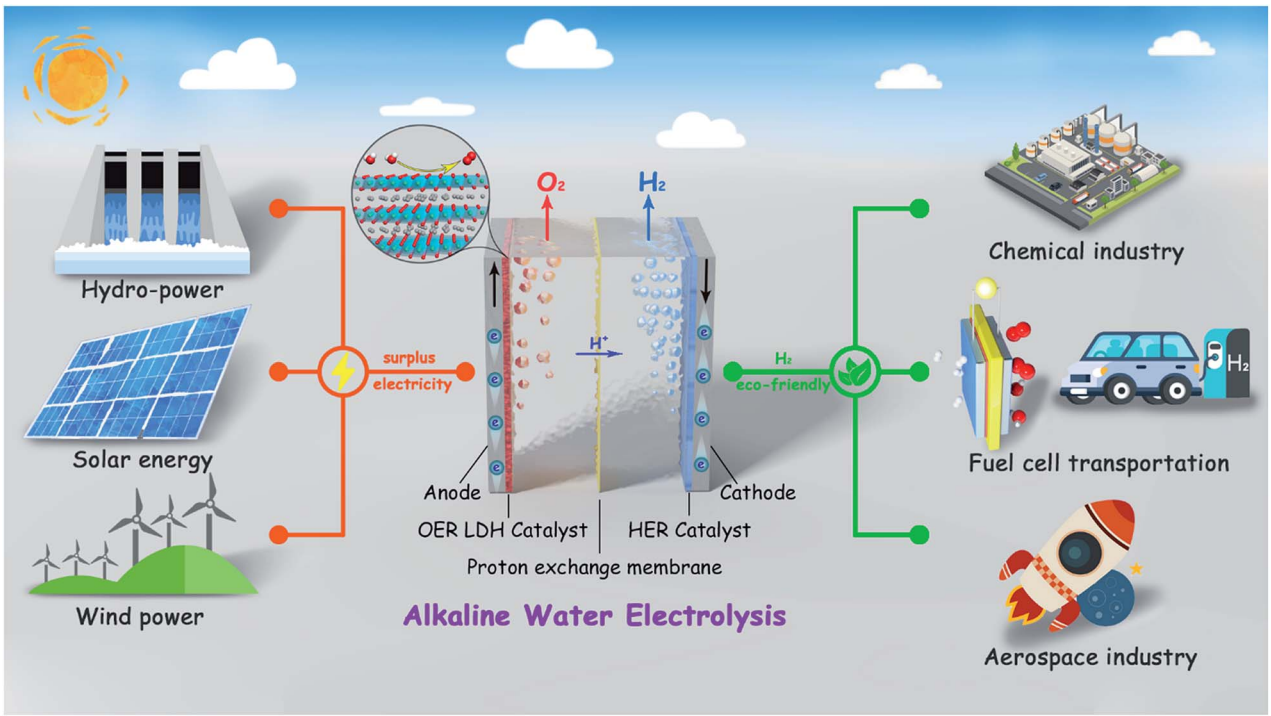

Fig. 1 A sustainable energy system based on an integrated water electrolysis system for renewable hydrogen fuel generation.

rare precious metals, studies have focused on exploring non-precious metal based new materials as OER electrocatalysts with low cost, high efficiency and stability. In these cases, great successes have been achieved in transition metal-based OER electrocatalysts, especially Fe, Co, and Ni,[23–26] such as their oxides,[27–35] phosphates,[36–38] selenides,[39–41] sulfides,[42–44] nitrides,[45–48] borides,[49–51] carbides,[52–54] and organometallic compounds.[55,56]

Among these transition metal based OER catalysts, layered double hydroxide (LDHs) nanosheets, belonging to the two-dimensional materials family, have attracted increased attention for the OER since 2013,[57] because of their numerous advantages such as large surface-to-bulk ratios, much more efficient exposure of catalytic active sites in comparison with 0D and 1D materials, controllable layered structure adjustment (intercalation, topological transformation, and assembly of other functional materials), tunable chemical composition with different cation ratios, hierarchical porosity facilitating the diffusion of water molecules and release of gaseous products, strong electrostatic interactions between layers and interlayer anions to offer an ordered arrangement of interlayer species and a tailorable orientation of active sites as well as the increase of structural stability. Yet, it remains challenging to overcome the poor conductivity, low electron and charge transfer ability and insufficient active edge sites, especially for the bulk form of LDHs.[58–60] Besides for water electrolysis, the use of LDH as a new promising class of compounds has already been well described in the literature for other fields of application, like adsorption,[61] photochemistry,[62] supercapacitors,[63] metal–air batteries,[64] and drug delivery.[65]

As illustrated in Fig. 2, LDHs have a layer-stacking crystal structure and the transition metals are located in the center of each octahedron with oxygen anions on the eight corners which is denoted as MO_6. These octahedrons form a 2D layer structure by edge-sharing. LDHs usually have a similar chemical formula of $[M^{II}_{1-x}M^{III}_x(OH)_2]^{x+}(A^{n-})_{x/n}\cdot mH_2O$,[66–68] consisting of a brucite-like $M^{II}(OH)_2$ layer in which part of the M^{II} cations are isomorphously substituted by M^{III} cations, and the positively charged bulk layers are filled with anions in order to achieve charge balance.[66,67] The positively charged layers are constructed by partially substituting monovalent cations (*e.g.*, Li^+), divalent cations (*e.g.*, Fe^{2+}, Ni^{2+}, Mg^{2+}, Ca^{2+}, Mn^{2+}, Co^{2+}, Cu^{2+}, and Zn^{2+}), or trivalent cations (*e.g.*, Al^{3+}, Co^{3+}, Fe^{3+}, Cr^{3+}, Ga^{3+} and Ti^{3+}). The intercalated anions are commonly filled by CO_3^{2-}, which can be replaced easily by other anions (*e.g.*, NO_3^-, SO_4^{2-}, ClO_4^-, Cl^- and Br^-).[68–71] The two-dimensional sheets arranged in a cross-type can make active sites fully and uniformly exposed, thus optimizing the catalytic performance.

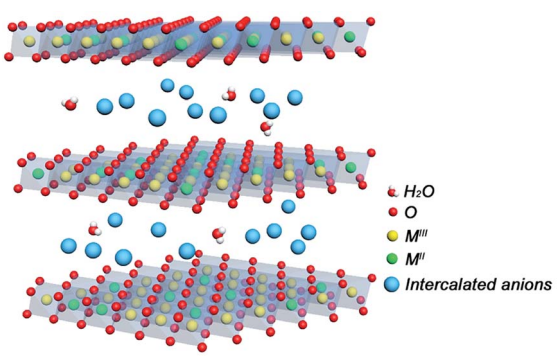

Fig. 2 Schematic diagram of the crystalline structure of LDHs.

Peer-reviewed publications on the structure, mechanism and related applications of LDH electrocatalysts have been already reviewed in the literature.[22,72–74] However, a review on the evolution of LDH materials deeply focusing only on water oxidation electrocatalysis by covering recent evaluation perspectives, the trends in the synthesis methods, a deep insight into the mechanism and the structure–activity correlation is urgently required. Thus in the review, we preferably focus on documenting the latest advances in LDH electrocatalysts for the OER in terms of key issues and developed strategies in designing LDH. The catalytic OER mechanism of LDHs and the performance evaluation parameters will be shortly introduced. Then we summarize the preparation methods with elaborated highlights on design strategies of LDHs. According to the chemical composition of transition metal components, developments and improvements on classification of different types of LDH catalysts are appraised comprehensively. Although there is still a gap between the performance of earth-rich OER catalysts developed so far and the theoretical prediction of the OER from water electrolysis, the LDHs summarized here provide a valuable reference for catalyst optimization and may lead to future breakthroughs in materials development.

1.1 OER mechanism of LDHs

With regard to the OER, the reaction processes of LDH electrocatalysts in alkaline solution are presented from eqn (3)–(7) for electrochemically splitting water. The corresponding multiple electron-transfer steps involved are illustrated in Fig. 3a. Each step needs to overcome the relative Gibbs free energy barrier (ΔG_n, $n = 1, 2, 3$ and 4), as shown in Fig. 3b.[75] The adsorption–desorption processes initiated at the active sites, *i.e.*, transition metal elements ([M]), subsequently generating [M–OH], [M–O] and [M–OOH] intermediates. The ΔG_3 indicates the step is thermochemically least favorable for the real OER catalyst, in which the OOH species is bound weakly to the catalyst.[75] The formation of M–OOH intermediates resulted in slow kinetics of the OER[76–79] and thus a high overpotential is usually required to prompt a positive OER.

$$[M] + OH^- \rightarrow [M\text{–}OH] + e^- \quad (3)$$

$$[M\text{–}OH] + OH^- \rightarrow [M\text{–}O] + H_2O + e^- \quad (4)$$

$$2[M\text{–}O] \rightarrow 2[M] + O_2 \quad (4.1)$$

$$[M\text{–}O] + OH^- \rightarrow [M\text{–}OOH] + e^- \quad (5)$$

$$[M\text{–}OOH] + OH^- \rightarrow [M\text{–}OO] + H_2O + e^- \quad (6)$$

$$[M\text{–}OO] \rightarrow [M] + O_2 \quad (7)$$

1.2 Key issues in designing LDH electrocatalysts

The performance evaluation parameters are summarized below which are commonly used to determine the effectiveness of OER electrocatalysts: overpotential (η), Tafel slope, turnover frequency, electrochemical surface area (ECSA) and stability.

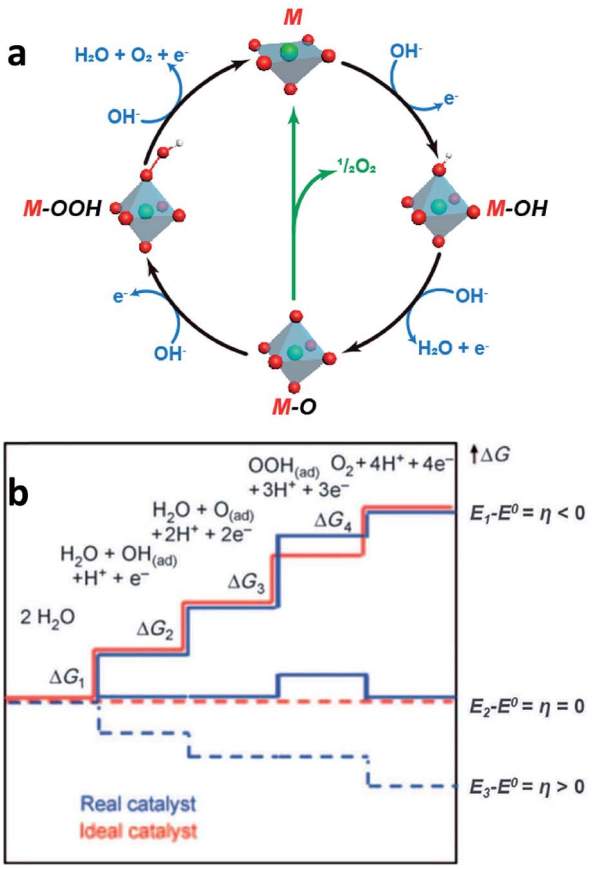

Fig. 3 (a) The OER mechanism of LDHs under alkaline conditions. The green line means the possible pathway of O_2 formation instead of M–OOH. (b) Plot of Gibbs free energy diagram of the OER *versus* the reaction coordination. Dashed lines indicate energetics at the electrode potential where all thermochemical barriers disappear ("thermochemical overpotential"). Reproduced with permission from ref. 75. Copyright 2010, Wiley-VCH Verlag GmbH & Co. KGaA, Weinheim.

1.2.1 Overpotential. To overcome the kinetic barriers imposed by the high activation energies for formation of reaction intermediates, the application of overpotential is essential to drive the electron transfer processes at a desired rate. According to the Nernst equation (eqn (8)), the applied potential required for electrolyzing water at 25 °C and pH = 0 can be calculated as $E_{eq} = 1.23$ V *vs.* NHE.

$$E_{eq(NHE)} = \frac{RT}{nF} \ln \frac{[Ox]}{[Red]} \quad (8)$$

(in which E_{eq} is the potential under equilibrium conditions, R is the ideal gas constant, T is the temperature in Kelvin, n is the number of moles of electrons, F is the Faraday constant, [Red] is the concentration of reduced molecules and [Ox] is the concentration of oxidized molecules.)

As the electrode potential changes with the pH, the reversible hydrogen electrode (RHE) has been utilized widely as a reference electrode at 25 °C (eqn (9)).

$$E_{eq(RHE)} = E_{eq(NHE)} + 0.059pH = 1.23 \text{ V} \quad (9)$$

The cell potential E can be expressed as eqn (10):

$$E_{(\mathrm{RHE})} = E_{\mathrm{test}} + E^0 + 0.059\mathrm{pH} \quad (10)$$

(in which $E_{(\mathrm{RHE})}$ is the converted cell potential, E_{test} is the applied potential, and E^0 is the cell potential under standard conditions).

Notably, different current densities will be referenced to different overpotential values. The overpotential value at a current density of $J = 10$ mA cm^{-2} (η_{10}) as a criterion was usually used. In this case, the smaller the value of η_{10} indicates the better electrocatalytic ability (eqn (11)).

$$\eta = E_{(\mathrm{RHE})} - E_{\mathrm{eq(RHE)}} \quad (11)$$

1.2.2 Tafel slope. Estimation of the Tafel slope is widely used to understand the Tafel behavior between electrocatalysts and reactants. By transforming the Tafel equation to a logarithmic function form (eqn (12)), a lower Tafel slope implies good electrocatalytic kinetics corresponding to the fact that the current density can increase faster with a smaller overpotential change, (*i.e.*, faster reaction rate constant). This provides valuable and insightful information toward the apparent OER mechanism, especially for elucidating the rate-determining step. As presented in Fig. 4, the electrocatalytic OER with small values of both the Tafel slope and η_{10} is ideal for practical purposes, that is, the higher OER activity of the electrocatalyst, the closer to the blue region in the bottom left corner of the figure.

Notably, the exchange current density (j_0) reflects the intrinsic rate of electron transfer kinetics between the analyte and the electrode. However, due to the complex OER pathways and large errors associated with their estimation,[80] j_0 is less concerned in the OER than in the HER.[23,81,82]

$$\eta = b \log\left(\frac{j}{j_0}\right) \quad (12)$$

(in which η is the overpotential, b represents the Tafel slope, j is the current density, and j_0 is the exchange current density.)

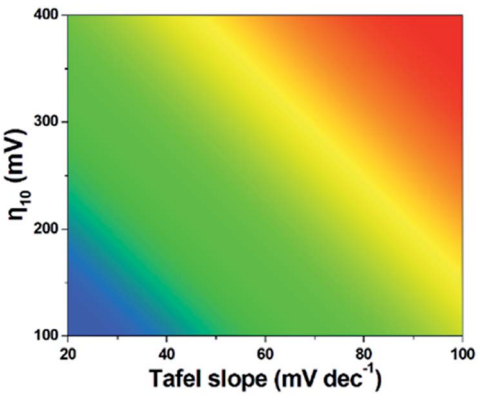

Fig. 4 Relationship between the Tafel slope and η_{10}, and evaluation mapping of the OER performance of LDHs.

1.2.3 Turnover frequency. Turnover frequency (TOF) quantifies the specific activity of catalytic centers. It is derived from the number of moles of O_2 produced per unit time per unit active site (eqn (13)).

$$\mathrm{TOF} = \frac{J \times A}{4 \times F \times m} \quad (13)$$

(in which J is the current density at a certain overpotential, A is the surface area of the catalyst, F is the Faraday constant, m is the number of moles of the active materials.)

1.2.4 Electrochemical surface area. The electrochemical surface area (ECSA) is also an important indicator, reflecting the absorption/desorption abilities of LDHs to water molecules and gaseous products, and the exposure of active sites. The ECSA value is proportional to the electric double layer capacitance (C_{dl}) of the working electrode, as described by eqn (14). The working electrode current (I) consists of two parts of I_{c} and I_{f}. Given the total current density of around zero and the small potential sweep range (usually 0.1 V), no chemical reaction occurs on the working electrode (eqn (15)), I_{f} can be ignored and C_{dl} remains unchanged. I_{c} can be expressed by eqn (16). By plotting the ΔJ against the scan rates, the linear slope of the resultant line is twice the C_{dl}.[83]

$$\mathrm{ECSA} = \frac{C_{\mathrm{dl}}}{C_{\mathrm{s}}} \quad (14)$$

(in which C_{s} is the specific capacitance value of a flat standard with 1 cm^2 of real surface area.)

$$I = I_{\mathrm{c}} + I_{\mathrm{f}} \quad (15)$$

(in which I_{c} is the double-layer current and I_{f} is the Faraday current.)

$$I_{\mathrm{c}} = \frac{\mathrm{d}q}{\mathrm{d}t} = \frac{\mathrm{d}(C_{\mathrm{dl}}\varphi)}{\mathrm{d}t} = C_{\mathrm{dl}}\frac{\mathrm{d}\varphi}{\mathrm{d}t} + \varphi\frac{\mathrm{d}C_{\mathrm{dl}}}{\mathrm{d}t} \approx C_{\mathrm{dl}}\frac{\mathrm{d}\varphi}{\mathrm{d}t} = C_{\mathrm{dl}}v \quad (16)$$

(in which q is the quantity of electric charge, φ is the potential, and v is the scan rate.)

1.2.5 Stability. Other than the activity parameters related to the kinetics and thermodynamics of OER catalysis, stability performance is another indispensable parameter. The cycling stability can be determined by the change in the linear sweep voltammetry (LSV) curve of the materials before and after at least 1000 cyclic voltammetric scans. The durability provides the change in performance at a certain current density or a certain potential as a function of reaction time. It is carried out in galvanostatic or potentiostatic mode for a very long time which usually extends up to several days. If the activity does not vary after such long-term polarization, the material can be regarded to be stable enough in OER electrolyzers.

1.2.6 Industrial application concerns. It is a long pathway from bench-scale research to commercialization. To meet the ultimate goal for industrial catalyst production, the awareness of energy, environment, and economy issues is also of great importance during the development of the integrated water electrolysis system, for example, the conversion efficiency of primary energy to secondary energy carriers, the cost-efficient preparation, the scale of electrode production with high

uniformity, and the environmental friendliness of preparation and electrolysis processes. Moreover, low-medium operating temperature (<60 °C), a mild electrolyte environment and safe working conditions should be also considered for the commercial development of water electrolysis systems,[84–86] especially for alleviation of the electrolytic corrosion problem.[87,88] The developed catalysts should be subjected to harsh stability tests, such as thousands of hours of chronopotentiometry or tens of thousands of cyclic voltammetry tests.

2 Design strategies for improving the OER performance of LDHs

In spite of the large number of transition metal based LDH electrocatalysts developed *via* optimizing synthetic parameters, the insufficient exposure of active sites, poor electron conductivity and weak ion transmission rate strictly limit the OER performance of LDHs.[89–91] To alleviate these problems, promising approaches explored are as follows: nanostructuring, hybrid LDHs with conductive materials, partial substitution of cations, interlayer anion replacement, vacancy creation and combination of computational methods and operando techniques.

In the section, typical synthetic methods and recently developed strategies in improving the OER performance of LDH electrocatalysts are highlighted and we will also discuss the relationships among synthesis, structure, properties and performance, as illustrated in Fig. 5. Research and development progress in various types of LDHs with a unique layered structure, adjustable layer spacing, controllable composition and diversity of anion filling is summarized in Table 1. In principle, the synthetic methods are relatively simple and the reaction is almost completed in one step, including hydrothermal/solvothermal reaction, co-precipitation, electrodeposition, or the combined procedures.[92–94] The hydrothermal/solvothermal reactions are the most widely applied by heating the desired precursors with deionized water or organic compounds (commonly dimethylformamide or methanol) as solvents. By controlling the synthetic parameters, like reaction temperature, time and pH, the morphology and structure can be easily controlled. The co-precipitation method involves the addition of a precipitant to a homogenous solution containing two or multiple metal cations. The precipitates can be readily collected after continuous post-treatments of aging, drying and/or calcining. However, the phenomena of particle agglomeration and insufficient particle uniformity commonly occur. The electrodeposition method is relatively simpler than the above-mentioned ones, which can complete preparation of LDHs in few minutes on the electrodes, such as metal foils, metal foams, carbon fiber paper, *etc.* Nevertheless, it remains challenging to finely control the morphological uniformity for a large-scale production.

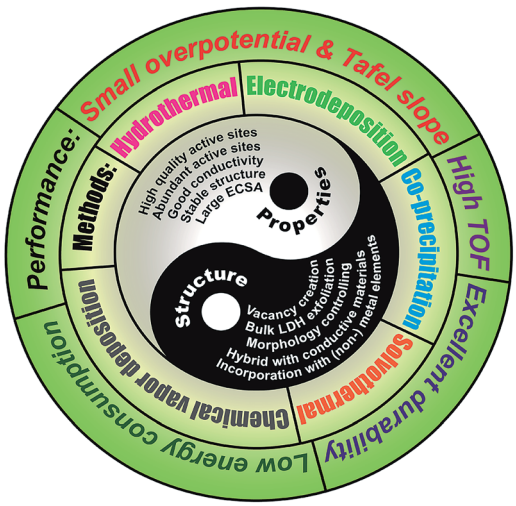

Fig. 5 Schematic representation of typical synthetic methods and development strategies of LDH OER electrocatalysts.

2.1 Nanostructuring

Nanostructuring is of great significance for maximizing the number of active sites *via* the increase of the surface areas and thus facilitating the diffusion of electrolyte and desorption of molecular oxygen. Shao and co-workers prepared NiFe LDH OER electrocatalysts with a hollow microsphere morphology composed of highly dispersed nanoplatelets (HMS), *via* template assisted growth using SiO_2 (Fig. 6a).[95] The current density of NiFe LDH HMS at an overpotential of 300 mV reached up to 71.69 mA cm^{-2}, which was 3.75 times higher than that of NiFe LDH nanoparticles (Fig. 6b). It was attributed to the constituent highly dispersed nanoplatelets with a high specific surface area, which was greatly beneficial to the exposure of surface active sites and also excellent hydrophilicity for adsorption of water molecules and release of oxygen molecules.

The fully occupied bonding t_{2g} orbitals of MO_6 centers in bulk LDHs probably lead to a low transfer of electrons and prohibit the reaction of an OH^- anion with an adsorbed O atom on catalytic active sites to form adsorbed –OOH species.[97] To address the problems of the dimensional confinement above, an alternative nanostructuring approach is to exfoliate bulk LDHs for increasing the quantity of active sites and optimizing the conductivity. Since the pioneering work by Hu's research group (Fig. 7a–c),[91] synthesis of various monolayered LDHs has been intensively conducted *via* a continuous liquid exfoliation technique, including topochemical treatment of CoCo and NiCo LDHs, hydrothermal processing of NiFe LDHs, exchange of interlayer anions, and finally exfoliation in formamide. As shown in Fig. 7d and e, the layer thickness of the exfoliated LDHs was reduced, and accordingly the edge lengths were increased, providing more active sites and thus enhancing the OER activities of the exfoliated LDHs under alkaline conditions, as compared to those of bulk LDHs. The trend of their OER activities was found to be in the sequence of NiFe > NiCo > CoCo for both exfoliated and bulk LDHs (Fig. 7f). In addition, the crystalline structure may also affect the catalytic activity. Lu and Zhao[96] investigated the effect of NiFe LDH crystallinity *via* annealing treatment (Fig. 6c). The amorphous NiFe LDH with

Table 1 Recent reports on the OER performance of LDH electrocatalysts

Catalyst	η_{10} (mV)	Tafel slope (mV dec^{-1})	Loading (mg cm^{-2})	Electrode	Electrolyte	Method	Ref.
CoFe LDHs							
$Ni_4Co_2Fe_3$ LDH	320	65	—	FTO[a]	1 M NaOH	CP[h]	24
$Ni_2Co_4Fe_3$ LDH	300	65	—	FTO	1 M NaOH	CP	24
$Ni_3Co_3Fe_3$ LDH	290	65	—	FTO	1 M NaOH	CP	24
Fe_1Co_1–ONS	350	36.8	0.36	GC[b]	0.1 M KOH	CP	110
CoFe LDH/rGO	396	43	0.204	GC	0.1 M KOH	CP & HT[i]	93
CoFe LDH@Cu NWs	240	44.4	1.8	—	1 M KOH	ED[j]	135
CoFe LDHs–Ar	266	37.85	0.2	NF[c]	1 M KOH	HT & Ar plasma	112
H_2O-plasma CoFe LDH	232	36	0.306	GC	1 M KOH	HT & H_2O plasma	114
E-CoFe LDHs	300	41	0.204	GC	1 M KOH	HT & HNO_3 etching	119
NiCo LDHs							
NiCo LDH	290	113	1.76	NF	0.1 M KOH	ST[k]	136
NiCo LDH NA/CFP	307	64	0.8	CFP[d]	1 M KOH	HT	83
NiCo LDH MS	409	96	0.8	CFP	1 M KOH	HT	83
Exfoliated NiCo LDH	367	40	0.17	CFP	1 M KOH	HT	71
Exfoliated NiCo NS	334	41	0.07	GC	1 M KOH	HT	91
$Ni_{76}Co_{24}$ LDHs	293	57	—	NF	1 M KOH	CP	137
CoNi LDH/CoO	300	123	0.265	GC	1 M KOH	CP	138
CoNiMn LDH/polypyrrole/RGO	369	77	0.2	GC	1 M KOH	CP	102
NiCo/NiCoOx@FeOOH	278	47.5	—	NF	1 M KOH	HT & hydrogenation & CP	94
NiFe LDHs							
$Fe_{0.1}Ni_{0.9}O$	297	37	0.022	Au/QCM[e]	0.5 M KOH	ST	139
O–NiCoFe LDH	420	—	0.12	GC	0.1 M KOH	CP	103
NiFeOx/CFP	250	31.5	1.6	CFP	0.1 M KOH	Dip-coating nostatic cycling	140
$Ni_{0.75}Fe_{0.25}$ LDH	350	64	0.143	GC	1 M KOH	HT	141
NiFe LDH HMS	239	53	0.25	GC	1 M KOH	HT	95
Exfoliated NiFe NS	302	40	0.07	GC	1 M KOH	HT	91
NiCoFe LDHs/CFC	239	32	0.4	—	1 M KOH	ED	104
NiFe LDH NS@DG10	210	52	0.283	GC	1 M KOH	Electrostatic stacking	142
NiFe LDH/RGO	245	—	1	CP[f]	1 M KOH	ST	143
NiFe LDH/N-rGO	258	63	0.36	NF	0.1 M KOH	ST	26
$Co_{0.85}Se$/NiFe LDH/EG	270 (η_{150})	57	—	—	1 M KOH	HT	144
NiFe LDH/CNT	247	31	0.25	CFP	1 M KOH	ST	57
Ni_8Fe LDH@CNTs	220	34	0.34	GC	1 M KOH	HT	145
NiFe LDH/CQD	235	35	0.2	GC	1 M KOH	ST	146
NiFe LDH/CQD	305	30	0.2	GC	0.1 M KOH	ST	146
3D NiFe LDH/Ni foam	230	50	—	—	0.1 M KOH	HT	99
$Ni_3FeAl_{0.91}$ LDH/Ni foam	304	57	0.5	—	1 M KOH	HT	100
NiFeMn LDH	270	47	0.2	CFP	1 M KOH	CP	101
$(Ni_{0.5}Fe_{0.5})_2P$/Ni foam	203	57	3	NF	1 M KOH	HT	147
MoFe : $Ni(OH)_2$/NiOOH/Ni foam	240	47	—	—	1 M KOH	HT	148
NiFe LDH@Cu NWs	199	27.8	—	—	1 M KOH	ED	149
NiFe LDH@Au/Ni foam	245 (η_{150})	48.4	—	—	1 M KOH	HT	150
NiFeRu LDH/Ni foam	225	32.4	1.2	NF	1 M KOH	HT	151
NiFe–Pt LDH	230	33	0.205	CC[g]	1 M KOH	HT & CP	92
Engraved NiFe-LDH	250	69	—	NF	0.1 M KOH	HT & flame	118
NiFe LDHs–V_{Ni}	229	62.9	0.204	GC	1 M KOH	HT & NaOH etching	115
NiFe LDHs–V_{Fe}	245	70	0.204	GC	1 M KOH	HT & NaOH etching	115
NiFe LDH–UF	254	32	0.35	CP	1 M KOH	CP & ultrasonication	117
Other LDHs							
$Ni_{0.75}V_{0.25}$ LDH	310	50	0.143	GC	1 M KOH	HT	141
NiMn LDH/rGO	260	46	2	NF	1 M KOH	HT	152
ZnNi LDH/N-rGO	290	44	0.18	GC	1 M KOH	ST	153
Ni_5Mn LDH/MWCNT	350	83.5	0.283	GC	1 M KOH	CP	154
CoMn LDH	325	43	0.142	GC	1 M KOH	HT	155
ZnCo LDH/Ni foil	520	83	—	—	0.1 M KOH	ED	156
Co_5Mn LDH/MWCNT	300	73.6	0.283	GC	1 M KOH	CP	154
Exfoliated CoCo NS	353	45	0.07	GC	1 M KOH	HT	91

Table 1 (*Contd.*)

Catalyst	η_{10} (mV)	Tafel slope (mV dec^{-1})	Loading (mg cm^{-2})	Electrode	Electrolyte	Method	Ref.
Precious metals							
20 wt% RuO_2/C	322	74	0.2	GC	1 M KOH	—	102
IrO_2	338	47	0.2	GC	1 M KOH	—	91
20 wt% Ir/C	370	78	0.2	CFP	1 M KOH	—	101

[a] Fluorine-doped tin oxide glass. [b] Glassy carbon. [c] Nickel foam. [d] Carbon fiber paper. [e] Quartz crystal microbalance. [f] Carbon paper. [g] Carbon cloth. [h] Co-precipitation. [i] Hydrothermal. [j] Electrodepostion. [k] Solvothermal.

a larger surface area and higher conductivity is more active than the crystalized ones for the OER (Fig. 6d).

2.2 Hybrid LDHs with conductive materials

As is well-known, it is not sufficient enough to solely increase the quantity of active sites. The other key tasks for improvement of the conductivity of LDHs have also gained a particular attention. Construction of hybrid LDH composites by growth of LDHs on conductive supports, like carbon or metal based materials, can greatly reduce the charge and electron transfer resistances, which may lead to a low Tafel slope.[98]

Gong and co-workers reported a solvothermal synthesis of ultra-thin NiFe-LDH nanosheets on slightly oxidized multi-walled carbon nanotubes (MWCNTs), as presented in Fig. 8a and b. Incorporation of MWCNTs significantly facilitated electron transport, thus improving OER activity and stability.[57] The η_{10} was only 247 mV and the Tafel slope was 31 mV dec^{-1}. In parallel, a great success was gained in the case of metal-based materials as supports, which inspired a great deal of research interest. Sun, *et al.* reported *in situ* growth of NiFe-LDHs on conductive nickel foam.[99] As shown in Fig. 8c, benefiting from the high conductivity of Ni foam supports, vertical NiFe-LDH nanosheets with a 3D porous structure exhibited a low onset overpotential of 230 mV with a Tafel slope of 50 mV dec^{-1}.

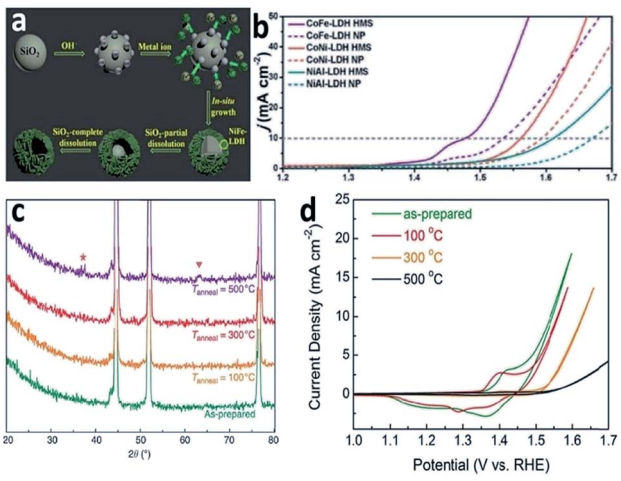

Fig. 6 (a) Scheme of the synthesis of NiFe-LDH HMS, and (b) polarization curves for CoFe-LDH, CoNi-LDH, NiAl-LDH HMS and NPs. Reproduced with permission from ref. 95. Copyright 2016, American Chemical Society. (c) XRD patterns of the as-prepared and annealed NiFe/NF samples. The pentagram and triangle represent the Bragg reflections for hematite. (d) Cyclic voltammograms (CVs) obtained in 0.1 M KOH solution at a scan rate of 5 mV s^{-1} with NiFe LDHs treated at different annealing temperatures. Reproduced with permission from ref. 96. Copyright 2015, Springer Nature Publishing AG.

2.3 Partial substitution of cations

An alternative approach to increase the quantity of active sites is partially substituting cations with foreign transition metals.

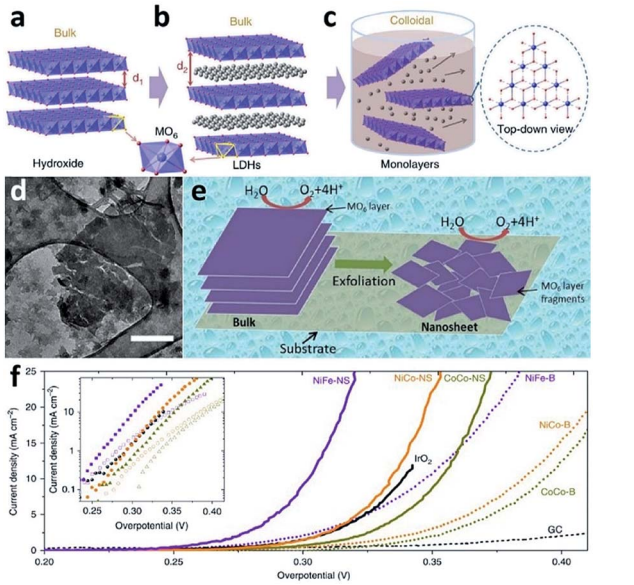

Fig. 7 Schematic representation of LDH structures, (a) layered hydroxides, (b) the incorporated LDHs with interlayer anions and water molecules, and (c) exfoliated LDH monolayers dispersed in a colloidal solution. Each single layer is composed of edge-sharing octahedral MO_6 moieties (M denotes transition metals). Transition metal atoms: purple spheres; oxygen atoms: red spheres; inter-layer anions and water molecules: grey spheres. Hydrogen atoms are omitted. (d) TEM image of a partially exfoliated NiCo LDH–NO_3^{2-} particle. Scale bar, 300 nm. (e) Illustration for the morphological change during exfoliation. Delamination of multilayered bulk LDHs particles into single layer nanosheets with a smaller size and a high number of overall edge sites. (f) Polarization curves. Inset shows the Tafel plots (conditions: scan rate was 5 mV s^{-1}, the loading was about 0.07 mg cm^{-2} for LDHs and 0.21 mg cm^{-2} for IrO_2 nanoparticles, 1 M KOH was used as the electrolyte). Reproduced with permission from ref. 91. Copyright 2015, Springer Nature Publishing AG.

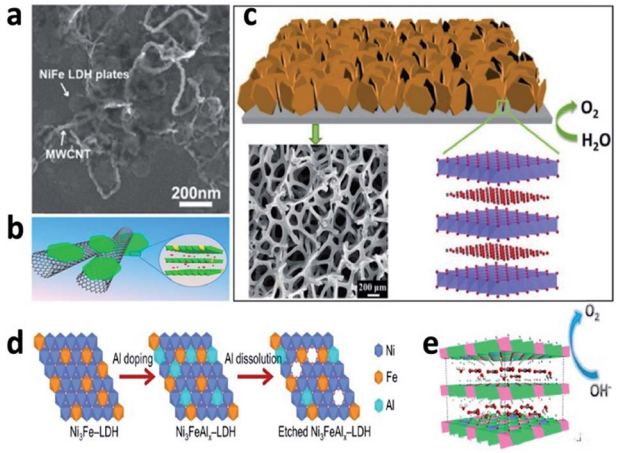

Fig. 8 (a) SEM image of NiFe-LDH nanoplates grown on mildly oxidized MWCNT networks, (b) the hybrid architecture and LDH crystal structure. Reproduced with permission from ref. 57. Copyright 2013, American Chemical Society. (c) Schematic illustration of NiFe-LDH nanoplates grown on nickel foam with the related SEM image of nickel foam and the crystal structure of LDHs. Reproduced with permission from ref. 99. Copyright 2014, The Royal Society of Chemistry. Partially substituted LTHs: (d) Ni_3FeAl_x-LDH. Reproduced with permission from ref. 100. Copyright 2017, Elsevier Ltd, and (e) NiFeMn-LDH. Reproduced with permission from ref. 101. Copyright 2016, The Royal Society of Chemistry.

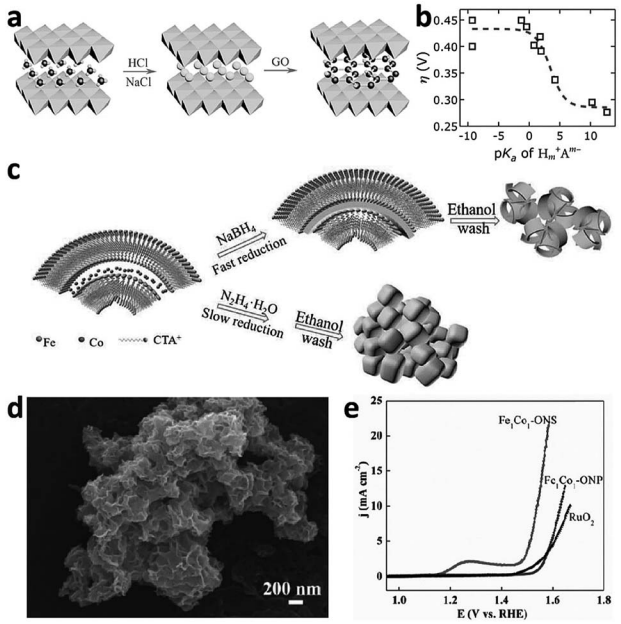

Fig. 9 (a) Fabrication process of FeNi–GO LDHs : FeNi–CO_3^{2-} LDHs were dispersed in a HCl and NaCl mixed solution and transformed into FeNi–Cl LDHs, which were further transformed into a FeNi–GO LDH hybrid by the anion exchange process. Reproduced with permission from ref. 108. Copyright 2014, Wiley-VCH Verlag GmbH & Co. KGaA, Weinheim. (b) Overpotentials of [NiFe]-LDH with different interlayer anions A^{m-} derived from constant current electrolysis at 1 mA cm^{-2} in a virtually carbonate-free electrolyte as a function of anion basicity. Open squares and dashed line stand for experimental data and sigmoidal fitting, respectively. Reproduced with permission from ref. 109. Copyright 2016, The Royal Society of Chemistry. (c) Schematic diagram of preparation of Fe_1Co_1–ONS and Fe_1Co_1–ONP (oxide nanoparticles), (d) SEM image of Fe_1Co_1–ONS, and (e) polarization curves of Fe_1Co_1–ONS, Fe_1Co_1–ONP, and RuO_2. Reproduced with permission from ref. 110. Copyright 2017, Wiley-VCH Verlag GmbH & Co. KGaA, Weinheim.

Partially substituted LDH materials have been widely investigated,[24,100–104] commonly leading to at least three types of cations, namely layered ternary hydroxides (LTHs) or ternary layered double hydroxides. As shown in Fig. 8d and e, by etching/dissolution of less stable and low coordination-number elements, structural defects and vacancies are generated in LDHs. Consequently, more active sites are exposed on the electrode surface.[25,100,105,106] For example, Guzmán-Vargas and co-workers developed Co^{2+} substituted NiFe-LDH materials *via* a co-precipitation method with tunable Co^{2+}/Ni^{2+} ratios.[24] The electrocatalysts exhibited a very low onset overpotential near 265 mV and a Tafel slope of 65 mV dec^{-1}. Particularly, the sample with an optimized atomic ratio of $Ni_3Co_3Fe_3$ achieved the best performance, that is, the lowest overvoltage of 250 mV. It was found that during the anode scan at a low potential, the Co^{2+} as a sacrificial electron acceptor can be firstly oxidized to Co^{3+}, preventing the oxidation of Ni^{2+} by Fe^{3+} and thus Ni^{2+} acted as the active sites for the OER.

2.4 Anion replacement

Replacement of interlayer anion components in LDHs not only facilitated the exfoliation process of bulk LDHs, but also improved the OER performance to some extent. Zhang and co-workers obtained single-layer CoAl LDH nanosheets by hydrothermal exfoliation of the bulk form in which a large number of CO_3^{2-} ions were included as interlayer anions.[107] The exchange of CO_3^{2-} by Cl^- or NO_3^- increased the interlayer distance of CoAl LDHs from 7.5 Å to 7.8 Å or 8.9 Å, respectively, and the large interlayer distance is beneficial for layers exfoliation. Similarly, the anion exchange approach was adopted for preparation of FeNi–GO LDHs from FeNi–CO_3^{2-} LDHs by Long and co-workers (Fig. 9a).[108] The enhanced electron transport arising from the strongly coupled GO resulted in superior electrocatalytic properties of FeNi–GO hybrids for the OER with overpotentials as low as 0.21 V. Hunter *et al.* also suggested that the Brønsted or Lewis basicity of the anions played a vital role in determining the OER mechanism.[109] The carbonates rapidly replaced other types of interlayer anions in alkaline electrolyte under ambient air. The OER activity of the LDHs is related to the pK_a of the conjugated acid of the interlayer anions (Fig. 9b). The higher charge of multivalent anions makes them stronger proton acceptors and electron donors than monovalent anions. It is possible that a strongly bound proton acceptor is required to reduce the activation barrier for water oxidation.[109]

2.5 Vacancy creation

The low coordinated catalytically active sites in LDHs possess lots of dangling bonds, which contribute to the catalytic activity improvement.[111,112] Much attention is thus being paid to the defect engineering of vacancy creation.[112–119] Typically,

vacancies can be mainly classified into three different types: anion vacancies (mostly in the form of oxygen vacancies), cation vacancies and multivacancies. Both oxygen and cation vacancies in electrocatalysts can finely tune the electronic properties of the surface. Oxygen vacancies can also decrease[114,118] or cation vacancies can increase[112,115] the valence state of nearby metal centers. As illustrated in Fig. 10, these methods are mostly used for creation of vacancy-rich LDHs: plasma etching,[112,114] thermal treatment,[118,120] aqueous chemical treatment[110,115,121] and sonication.[117]

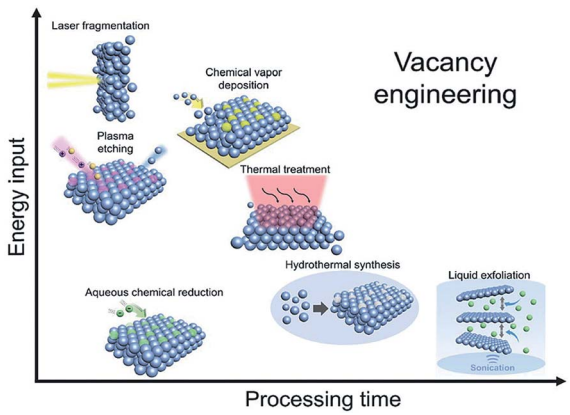

Fig. 10 Schematic presentation of vacancy creation techniques for transition metal-based electrocatalysts. Reproduced with permission from ref. 116. Copyright 2018, Wiley-VCH Verlag GmbH & Co. KGaA, Weinheim.

Wang *et al.* prepared for the first time defective CoFe LDHs *via* a water-plasma-enabled exfoliation strategy.[114] Multivacancies (O, Co and Fe vacancies) during the exfoliation process were generated as verified by HRTEM (Fig. 11a and b) and Fourier-transform extended X-ray absorption fine structure (FT-EXAFS). The coordination number (*N*) of Co–OH and Co–M (M = Co or Fe) in plasma-exfoliated samples was smaller than that in pristine samples (Fig. 11c), leading to the significant enhancement of catalytic activity (Fig. 11d). Corroboratively, the authors found that by aid of Ar plasma etching, favorable multiple vacancies can also be created during exfoliation of bulk CoFe LDHs into ultrathin nanosheets.[112]

2.6 Combination of computational methods and operando techniques

Notably the plausible assumptions of the relationships between the structures of catalysts and the active sites may lead to erroneous conclusions. It remains problematic to correlate theoretical and experimental aspects as due to the realistic conditions (solvent, electric field, *etc.*) and kinetics. Therefore it is urgently necessary to combine theoretical studies with experimental approaches for the building-up of the relationships among the structure, activity and mechanism.[60] The combination of theoretical simulations (density functional theory (DFT) computation) and advanced *in situ* characterization techniques (*in situ* spectroscopy and microscopy) has been developed to study the origin of catalyst activity and is helpful to further analyze the OER processes, since the reports of the

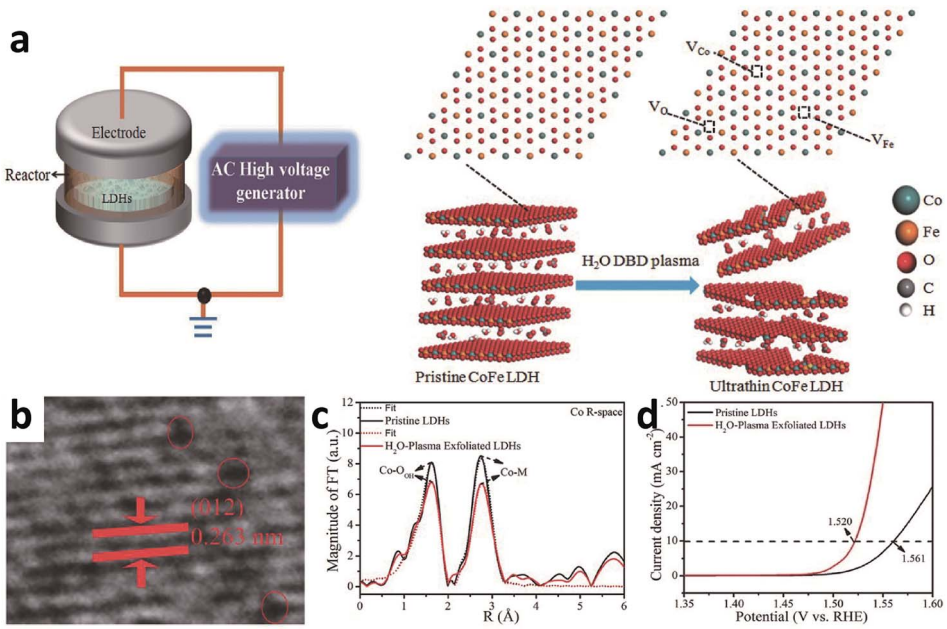

Fig. 11 (a) Schematic illustration of water-plasma-enabled exfoliation of CoFe LDH nanosheets. The dielectric barrier discharge plasma reactor was equipped with a plate-to-plate electrode at 50 V powered by an AC high voltage generator. (b) HRTEM images of the water-plasma exfoliated CoFe LDH nanosheets. (c) Co K-edge FT-EXAFS of pristine and water-plasma exfoliated CoFe LDH nanosheets with homologous curve-fitting results. (d) LSV curves for the OER on pristine CoFe LDHs and the water-plasma exfoliated CoFe LDH nanosheets. Reproduced with permission from ref. 114. Copyright 2017, Wiley-VCH Verlag GmbH & Co. KGaA, Weinheim.

pivotal role of Fe ions on the activity increase of Ni or Co (oxy) hydroxides by Boettcher *et al.*[122–127]

Friebel *et al.* employed *in situ* X-ray absorption spectroscopy (XAS) to establish the local environment of Ni and Fe cations in $Ni_{1-x}Fe_xOOH$, which was also one of the earliest pieces of evidence for Fe as the active site in $NiFeO_x$ by DFT computations.[128] The authors found that the γ-FeOOH phase nucleated when the atomic content of Fe was increased above 25%, in which the Fe K-edge high energy resolution fluorescence detection (HERFD) XAS spectra showed strong potential-induced phase changes (Fig. 12a and b), and a 500-fold enhancement in OER activity was observed as compared to pure Ni and Fe oxyhydroxide films. The DFT + U calculations revealed that the Fe sites had a theoretical overpotential of about 0.43 V while the Ni sites had an overpotential of 0.59 V (Fig. 12c).Zhang *et al.* fabricated single-atom Au supported NiFe LDH (^{S}Au/NiFe LDH) (Fig. 12d). To understand the original activity at an atomic level, the free energy difference of adsorbed intermediates (OH*, O*, and OOH*) on the single active site was simulated.[129] The rate-determining step was determined to be the formation of OOH* from O* with an overpotential of 0.18 V (Fig. 12e). Stahl *et al.* provided the first direct evidence of Fe^{4+} species in NiFe oxyhydroxide during the OER by operando Mössbauer spectroscopy (Fig. 12f).[130] When increasing the potential to 1.62 V, the appearance of a shoulder in the Mössbauer spectra can be interpreted as the oxidation of Fe^{3+} to Fe^{4+} (Fig. 12g). Observation of Fe^{4+} in NiFe LDH, but not in the Fe-only one, was attributed to the stabilizing effect of the NiOOH lattice. Although the Fe^{4+} species were not directly responsible for the catalytic activity, the presence of reactive (unobserved) Fe^{4+} species generated at the edge, corner, or related defect sites within the Fe-doped NiOOH lattice was proposed to be favorable for water oxidation processes.

3 Recent developments and improvements on LDH OER electrocatalysts

Transition metal-based LDH materials, especially containing the group VIII elements when introducing recent strategies for preparation, have already been covered above. Therefore, the section summarizes the recent developments and improvements in the compositional classification of LDH materials, as listed in Table 1. The obtained performance evaluation parameters have been also tabulated for comprehensive understanding and comparison.

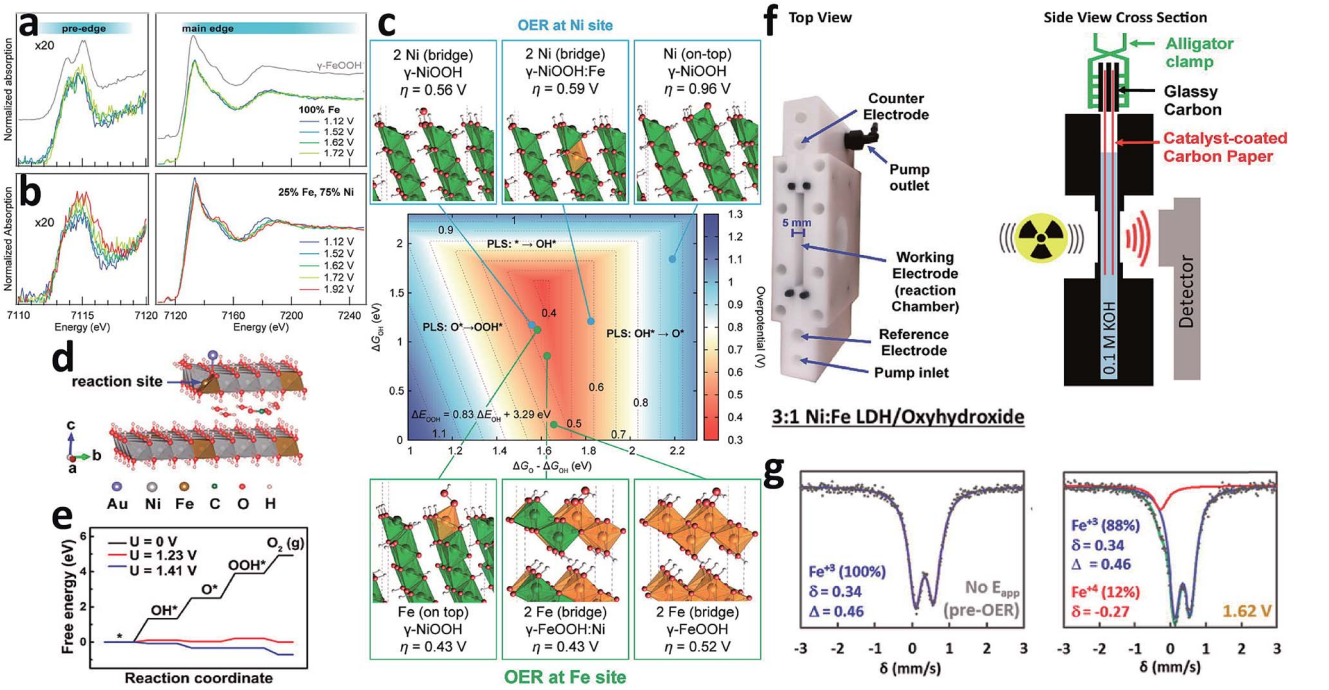

Fig. 12 Comparison of the 100% Fe-containing sample with OER catalysts containing 25% Fe and 75% Ni using operando HERFD XAS. (a) The catalyst containing 100% Fe. The spectrum of γ-FeOOH is also shown for comparison. Plots of both pre-edge (enlarged) and the full spectra are shown. (b) Fe K-edge. While the potential increase does not influence the oxidation-state-sensitive energy of the main absorption threshold (7125 eV), significant contraction of the Fe–O bond with increasing potential is clearly indicated by the changes of the photoelectron scattering features (energy range above 7140 eV). (c) Theoretical OER overpotentials at Ni and Fe surface sites in pure and doped γ-NiOOH and γ-FeOOH model structures. Reproduced with permission from ref. 128. Copyright 2015, American Chemical Society. (d) Two-layer slab model for ^{S}Au/NiFe LDH with interlayer CO_3^{2-} anions and water molecules. (e) Free energy diagram for the OER at different potentials on the surface of the ^{S}Au/NiFe LDH model. Reproduced with permission from ref. 129. Copyright 2018, American Chemical Society. (f) Top view and side-view cross-sectional schematic of the operando Mössbauer-electrochemical cell. (g) Mössbauer spectra of NiFe LDH at the resting state (open circuit, left) and at 1.62 V *vs.* RHE (OER conditions, right). Reproduced with permission from ref. 130. Copyright 2015, American Chemical Society.

3.1 Cobalt/iron based LDHs

The OER performance of a desirable electrocatalyst can be described as the e_g occupancy of surface transition-metal cations close to unity.[131] Cobalt/iron based LDHs (CoFe LDHs) have recently gained tremendous attention because of the electronic configuration of Co^{2+} ($t_{2g}^6e_g^1$) being near the optimal e_g filling.[93,132,133]

Synthesis of cobalt iron oxide nanosheets (Fe_xCo_y–ONS) *via* a simple solution reduction method using $NaBH_4$ as a reducing agent was studied by Zhuang and co-workers (Fig. 9c).[110] Fe_1Co_1–ONS exhibited an overpotential of 350 mV at a current density of 10 mA cm^{-2} (Fig. 9d and e) with a Tafel slope of 36.8 mV dec^{-1}. After the stability test for 10 000 s, the current density of Fe_1Co_1–ONS was increased by 11.2%. By aid of X-ray photoelectron spectroscopy (XPS), a notable increase was observed in both the ratios of Co^{2+}/Co^{3+} and concentration of the O component element at a binding energy of 531.6 eV for Fe_1Co_1–ONS, revealing the generation of more oxygen vacancies during the electrochemical process. The ultra-thin nanosheet structure increased the number of active sites and contributed to the dispersion and transport of OH^-. Moreover, the oxygen vacancies can enhance the conductivity and promote the adsorption of water molecules on active Co^{3+} sites.

Based on DFT + U calculation data, Bell and coworkers in 2013 pointed out that the overpotential for β-CoOOH can be reduced by substitutional doping of Co active sites by transition metal cations, like iron.[134] To verify the effect of iron experimentally, Burke *et al.* in 2015 studied the stepwisely substituted Fe in CoOOH. The OER activity of the electrodeposited $Co_{1-x}Fe_x(OOH)$ with $x \approx 0.4$–0.6 was an ~100 times enhancement ($TOF_{mass} = 0.61 \pm 0.10\ s^{-1}$), compared to that of CoOOH ($TOF_{mass} = 0.007 \pm 0.001\ s^{-1}$). CoOOH provided a conductive, chemically stable, and intrinsically porous/electrolyte-permeable host for Fe, and Fe sites were proved to be the most dominant active sites for the OER (Fig. 13a–c).[127] Moreover, the role of Fe was also found to be vital for chemical stability. Essentially, when x is smaller than 0.54, the films were chemically stable, despite the dramatic drop in the OER activity within 2 h. In contrast, when $x \geq 0.54$, the film was dissolvable in alkaline electrolyte during the OER.

By combination of CoFe-LDHs with reduced graphene oxide (RGO), Han *et al.* observed that the fabricated 2D lamellar CoFe-LDH/RGO nanohybrids with enhanced mass/charge transfer capability and structural stability achieved $J = 10$ mA cm^{-2} at an overpotential of 325 mV and good durability for 10 h at $J = 10$ mA cm^{-2} (Fig. 13e and f).[93] The incorporated Fe led to a broader interlayer space. The synergistic interactions between RGO with Co and Fe species improved the conductivity and shortened the ion transfer distance (Fig. 13d).[93]

3.2 Nickel/iron based LDHs

Nickel/iron based LDHs (NiFe LDHs) are one of the most investigated LDHs because of their low synthetic cost, low

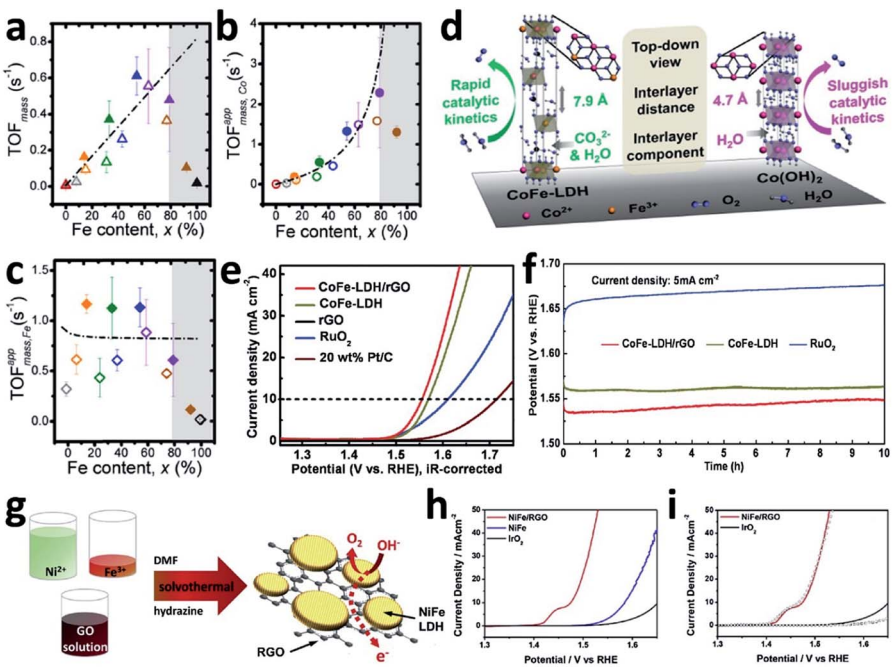

Fig. 13 TOF data depicted based on assuming total film mass and composition: (a) all metal sites are available for catalysis (TOF_{mass}, triangles), (b) Only Co-sites are available for catalysis ($TOF^{app}_{mass,Co}$, circles), and (c) only Fe-sites are available for catalysis ($TOF^{app}_{mass,Fe}$, diamonds) during steady-state polarization at $\eta = 350$ mV after 1 min (closed symbols) and 120 min (open symbols). Dot-dash lines (a–c) are calculations. Reproduced with permission from ref. 127. Copyright 2015, American Chemical Society. (d) Schematic of the crystalline structures of CoFe-LDH nanosheets and $Co(OH)_2$, (e) iR-corrected polarization curves, (f) chronopotentiometry curves on a GC electrode at $J = 5$ mA cm^{-2}. Reproduced with permission from ref. 93. Copyright 2016, Wiley-VCH Verlag GmbH & Co. KGaA, Weinheim. (g) Schematic illustration of the synthetic method and formed NiFe LDH on RGO supports for oxygen evolution, (h) polarization curves, and (i) stability measurements (empty circles and rectangles indicated the polarization curves of each catalyst after 1000 cycles). Reproduced with permission from ref. 143. Copyright 2015, Elsevier B.V.

toxicity, and environmental friendliness.[139] NiFe LDHs show the best performance for electrochemical OER,[91,125,157,158] compared to other transition metal based catalysts and even the precious metal catalysts such as IrO_2 and RuO_2.[99,108] Subbaraman *et al.* systematically investigated four different types of 3d transition metal (oxy)hydroxides. Their OER activities were demonstrated to be in the order of Ni > Co > Fe > Mn, in accordance with the OH_{ad}–$M^{2+\delta}$ energetic strength order of Ni < Co < Fe < Mn.[159] As for doping of NiFe LDHs, Trotochad *et al.* found that Fe self-doping led to the disordered crystal structure of γ-NiOOH,[124] and also contributed to the conductivity enhancement, being beneficial for improvement of the OER activity of $Ni_{1-x}Fe_x(OH)_2$/$Ni_{1-x}Fe_xOOH$.[22] Lee *et al.* deposited NiFe LDHs uniformly on reduced graphene oxide (RGO) *via* a simple one-pot solvothermal method (Fig. 13g).[143] With the help of RGO as a support, the electrocatalyst showed a lower overpotential of 245 mV at $J = 10$ mA cm^{-2} and a long-term electrochemical stability (Fig. 13h). After 1000 cycles of potential sweeps, the loss in activity was negligible (Fig. 13i). The RGO with a large surface area was greatly beneficial for loading LDHs and also providing electrical and mass pathways. The intimate contact between the NiFe LDHs and RGO layers played an important role in electron transfer. By mixing Ni and Fe precursor salts with GO and protonated g-C_3N_4 nanosheets (p-CNNS), Hou *et al.* prepared NiFe LDHs/nitrogen doped RGO (NiFe LDHs/NRGO) by a simple solvothermal reaction.[26] It displayed an overpotential of 258 mV at $J = 10$ mA cm^{-2}, a bit higher than that of NiFe LDHs/RGO (250 mV). However, the lowest Tafel slope of 63 mV dec^{-1} was obtained on NiFe LDHs/NRGO as compared to pristine NiFe LDHs (143 mV dec^{-1}), NiFe-LDHs/RGO (91 mV dec^{-1}) and even IrO_2 (81 mV dec^{-1}). The improvement in catalytic activity was mainly ascribed to the enhanced electron-donor property by N-doping and the formation of nitrogen-containing active sites. Fabrication of NiFe LDH/CQD composite was also reported by Kang and Liu, *et al. via* a one-step solvothermal method.[146] The conductive CQDs with a size of about 5 nm significantly

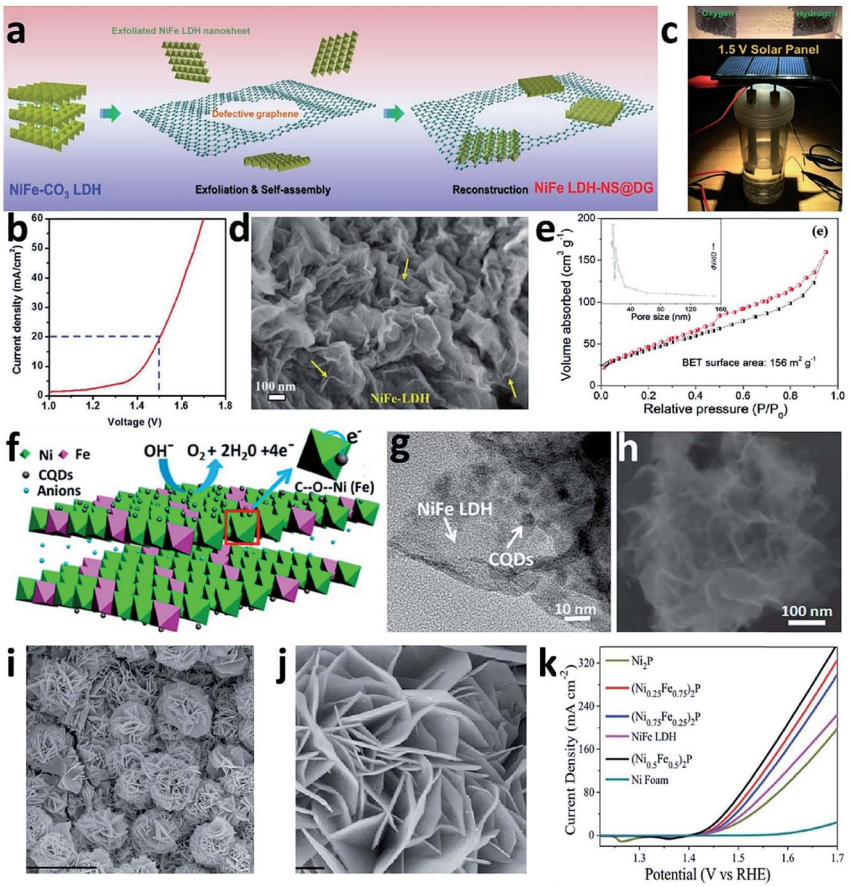

Fig. 14 (a) Schematic illustration of the preparation of NiFe LDH-NS@DG nanocomposites, (b) LSV curve of NiFe LDH-NS@DG10 as an OER and HER bifunctional catalyst in 1 M KOH for overall water splitting (both loaded into Ni foam at a loading of 2 mg cm^{-2}), (c) demonstration of a solar power assisted water-splitting device with an external voltage of 1.5 V. Reproduced with permission from ref. 142. Copyright 2017, Wiley-VCH Verlag GmbH & Co. KGaA, Weinheim. (d) FESEM images of EG/$Co_{0.85}Se$/NiFe-LDH, and (e) N_2 adsorption isotherm and the corresponding pore size distribution (inset) of EG/$Co_{0.85}Se$/NiFe-LDH. Reproduced with permission from ref. 144. Copyright 2016, The Royal Society of Chemistry. (f) Schematic model of the roles of CQDs in the high electrocatalytic activity of CQD/NiFe-LDH nanocomposites, (g) SEM image of the CQD/NiFe-LDH, and (h) TEM images of the CQD/NiFe-LDH hybrid. Arrows point to individual NiFe-LDH plates and smaller CQD particles. Reproduced with permission from ref. 146. Copyright 2014, American Chemical Society. (i and j) SEM images of $(Ni_{0.5}Fe_{0.5})_2P$ microflowers, and (k) polarization curves of $(Ni_xFe_{1-x})_2P$, NiFe LDH, Ni_2P and Ni foam (iR-corrected), at a scan rate of 0.1 mV s^{-1}. Scale bars: (i) 10 μm; (j) 500 nm. Reproduced with permission from ref. 147. Copyright 2017, The Royal Society of Chemistry.

enhanced the conductivity, electron transfer and electron storage properties of NiFe LDHs (Fig. 14f–h), exhibiting a high OER activity of $\eta_{10} = 235$ mV in 0.1 M KOH.

Furthermore, Yao and co-workers reported exfoliated NiFe LDH nanosheets (NS)/defective graphene (DG) by electrostatic stacking of positively charged NiFe LDH NS and negatively charged DG (Fig. 14a).[142] The OER electrocatalytic activity in alkaline solution was further enhanced with an overpotential of 210 mV at $J = 10$ mA cm^{-2}. The different types of DG derived by the removal of heteroatoms from graphene acted as active sites, directly capturing the transition metal atoms *via* strong π–π interaction and thus contributing to activity improvement for three basic electrochemical reactions (*e.g.*, the ORR, OER and HER).[160] Moreover, NiFe LDH-NS@DG also showed a good ability for electrochemical overall water-splitting (Fig. 14b and c).[142]

A challenge was encountered in exploiting high-performance electrocatalysts, Feng and co-workers thus designed a ternary EG (exfoliated graphene foil)/$Co_{0.85}Se$/NiFe-LDH hybrid.[144] The NiFe-LDHs grown on EG/$Co_{0.85}Se$ nanoarrays were estimated to be about 10 nm in thickness as shown in the field emission scanning electron microscopy (FESEM) images (Fig. 14d). The ternary hybrid catalyst with a high surface area of 156 m^2 g^{-1} exhibited a J of 150 mA cm^{-2} and 250 mA cm^{-2} at the overpotentials of 270 mV and 280 mV, respectively (Fig. 14e). A competent OER stability was also observed, showing an anode current density of 200 mA cm^{-2} at 1.52 V (*vs.* RHE) for more than 10 h without significant decrease. Furthermore, by use of the catalysts both as the cathode and the anode, a current density of 20 mA cm^{-2} was achieved at an external voltage of 1.71 V for overall water splitting in a two-electrode cell. The excellent performance was attributed to the inherent properties and strong coupling effects of the three components, ensuring low charge transfer resistance and fast vectorial electron-transport. The 3D layered structure could offer large amounts of active sites and accelerate gas bubble release.[144]

In addition to being supported on carbon materials, the growth of NiFe LDHs on metal based current collectors (metal foams and foils), has been investigated to reduce the interface resistance and promote strong gas release from the OER process. For instance, Luo *et al.* fabricated nickel iron phosphide mixed microflowers ($(Ni_xFe_{1-x})_2P$) with a 3D ternary micron-sized molecular porous structure on nickel foam by a hydrothermal method and phosphating treatment (Fig. 14i and j).[147] Owing to the unique 3D hierarchical structures and strong synergy effects between Fe, Ni and P, a current density of 20 mA cm^{-2} at a low overpotential of 219 mV was achieved (Fig. 14k).

Another interesting fabrication strategy was to synthesize 3D core–shell structured NiFe LDHs on Cu nanowires (NWs), as reported by Yu and co-workers (Fig. 15a and b).[149] Cu NWs were firstly grown on Cu foam *via* a chain of methods including chemical oxidation, calcination and electronic reduction. The NiFe LDH shells were electrolytically deposited on Cu NWs. A current density of 10 mA cm^{-2} was achieved on the electrocatalyst at an overpotential of 199 mV and the Tafel slope was only 27.8 mV dec^{-1} (Fig. 15c and d). The two-electrode cell configuration consisted of a Cu@NiFe LDH electrode as both the anode and cathode for efficient overall water splitting, achieving $J = 10$ mA cm^{-2} and 100 mA cm^{-2} at 1.54 V and 1.69 V, respectively. The outstanding catalytic activity of Cu@NiFe LDH was attributed to the following merits: (1) NiFe

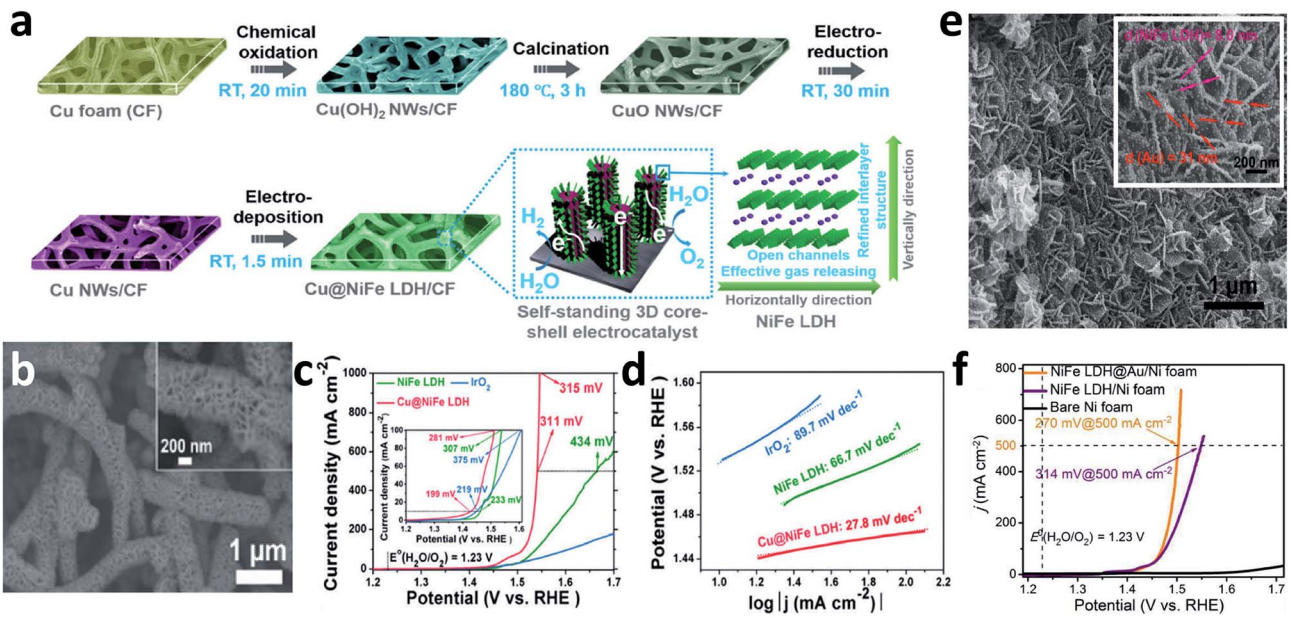

Fig. 15 (a) Schematic illustration of fabrication of self-standing 3D core–shell Cu@NiFe LDH electrocatalysts (RT is the abbreviation of room temperature), (b) SEM images of Cu@NiFe LDH, (c) the corresponding polarization curves and (d) Tafel plots. Reproduced with permission from ref. 149. Copyright 2017, The Royal Society of Chemistry. (e) SEM images for NiFe LDH@Au/Ni foam, and (f) polarization curves of NiFe LDH@Au/Ni foam (at a scan rate of 2 mV s^{-1}), NiFe LDH/Ni foam and bare Ni foam (at a scan rate of 5 mV s^{-1}). Reproduced with permission from ref. 150. Copyright 2017, American Chemical Society.

LDHs were tightly attached to Cu NWs. The latter was directly grown on Cu foam without using any extra binder, thus ensuring good conductivity and mechanical stability, (2) formation of a 3D core–shell structure increased the exposure of edge sites in LDHs, and the appropriate interlayer space of LDH layers can ensure intimate contact between the catalyst and the electrolyte, and facilitates desorption of gas products.[149]

Besides optimization of OER performance by coupling NiFe LDHs with conductive supports, further introduction of noble metal elements with LDHs can increase the catalytic activity. Zhu *et al.* reported the chemical deposition of Au on NiFe LDHs@Ni foam, showing a robust OER performance in alkaline solution (Fig. 15e).[150] When the overpotentials of 221, 235 and 270 mV were provided, the current densities of 50, 100 and 500 mA cm^{-2} were observed, respectively (Fig. 15f). The ultrahigh OER catalytic activity was explained by: (1) the unique multilevel topology consisting of a 3D macroporous nickel framework covered by high density upright hybrid nanoarrays, plenty of exposed active sites and promoted electrolyte diffusion and accelerated gas bubble release, (2) the highly electronegative metal of Au acted as an electron adsorbent to generate and stabilize the high oxidation state of nickel cations (Ni^{3+}), and thus improved the OER efficiency,[161] (3) strongly electrophilic Ni^{3+} would promote the formation of the dominant oxyhydroxide (OOH) species for O_2 evolution; (4) the improved conductivity and large surface area of NiFe LDH@Au/Ni foam; (5) the increase in surface roughness caused by acid etching during a preparation procedure, contributing to the increase of the active surface area. Based on the combination of the excellent adsorption abilities of Ru toward both hydrogen- and oxygen- containing intermediates,[162] Zhang and co-workers tailored the water-splitting active sites of NiFe-LDH through partial substitution of Fe centers by Ru dopants.[151] The Ru doped catalyst not only exhibited excellent OER activity, but also showed outstanding HER activity under alkaline conditions. A current density of 10 mA cm^{-2} at a cell voltage of 1.52 V for overall water splitting was obtained, which was far lower than the voltage of the Pt/C–Ir/C couple electrode (1.60 V).[151]

Zhou *et al.* reported that an abundance of oxygen vacancies can be created in the NiFe-LDH structure (Fig. 16a)[118] by a fast flame treatment in which the flame core can provide a reducing (low oxygen) and high-temperature environment. The oxygen vacancies can provide an electron-rich structure of metal sites and delocalized electrons, showing a negative shift of both Fe 2p (Fig. 16b) and Ni 2p peaks as confirmed by the XPS results. The synergistic modulation of abundant oxygen vacancies, low coordination number and electron-rich structure contributed to the enhanced OER performance (Fig. 16c). By using DFT + U simulation, the Gibbs free energy changes indicated the facile adsorption of OH^- on bridge sites and the decreased energy barrier from OH* to O* over the NiFe-LDH sample with the presence of oxygen vacancies. However in pristine LDH, only Fe species would act as the active sites. A more kinetically favorable mechanism was proved over the oxygen vacancy-rich NiFe-LDH, showing a smaller overpotential of 0.84 eV for the OER (Fig. 16d).

3.3 Nickel/cobalt based LDHs

Ni/Co-based LDHs are another promising catalyst candidate for the OER with the advantages of their unique electronic

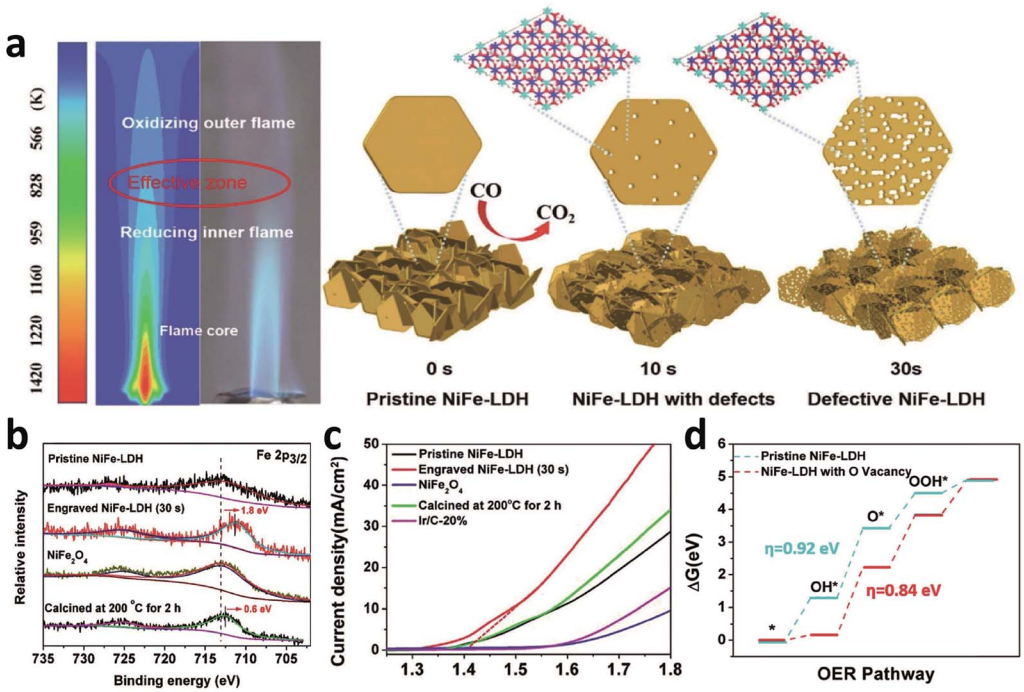

Fig. 16 (a) Temperature distribution simulation of flame and morphology change of NiFe LDH treated with flame for different periods of time, (b) XPS characterization of Fe sites, (c) iR-corrected polarization curves, and (d) the calculated OER free energy on NiFe-LDH with/without the present of oxygen vacancies. Reproduced with permission from ref. 118. Copyright 2018, Wiley-VCH Verlag GmbH & Co. KGaA, Weinheim.

properties, edge-sharing octahedral MO_6 crystal structures and tunable chemical compositions.[69,138,163] The electronic configurations of Co^{3+} and Ni^{3+} are most likely $t_{2g}^5e_g^1$ and $t_{2g}^6e_g^1$, respectively, in accordance with the maximum OER activity of transition metals at an e_g occupancy close to unity.[138]

A Ni/Co layered double hydroxide (NiCo LDH) had been directly grown on Ni foam *via* a solvothermal process by Jiang and co-workers.[136] The catalyst exhibited superior OER performance in alkaline solutions with an onset potential of 290 mV, and reached $J = 10$ mA cm^{-2} at an overpotential of 420 mV which was slightly higher than that of a RuO_2 catalyst (410 mV) (Fig. 17a and b). The performance can be attributed to the intrinsic layered structure of LDHs with large interlayer space, facilitating the diffusion of hydroxide groups and water molecules. Direct growth of layers on Ni foam could not only offer a stable structure, but also improve the electrical conductivity. The authors also pointed out that the high valence cations of Ni and Co ($Ni^{3+/4+}$ or $Co^{3+/4+}$) were identified to be the key active sites for the OER. Yu *et al.*[83] found that the metal salt solution containing Ni and Co would form a microsphere structure (NiCo-LDHs-MS) when the carbon fiber paper (CFP) was absent after hydrothermal treatment, whereas with a CFP support, the nanoplate array structure of NiCo-LDH (NiCo-LDH-NA) was formed. NiCo-LDH-NA showed a low overpotential of 307 mV at $J = 10$ mA cm^{-2} and a low Tafel slope of 64 mV dec^{-1}. In contrast, the NiCo-LDH-MS possessed fewer active sites and slower mass transport during the electrochemical process. Li *et al.*[137] found the molar ratio of Ni and Co ions played a key role in the OER activity of NiCo LDHs. When the relative ratio of Ni/Co ions was tuned to be 2 : 1, the formed $Ni_{76}Co_{24}$-LDHs exhibited the best OER activity, that is, a low onset overpotential of 242 mV and excellent stability maintaining 92.1% of the initial current density after being tested for 10 000 s. It was attributed to the unique mesoporous tremella-like structure, the synergistic effect of Ni and Co with the optimized proportion and an appropriate electronic configuration. A novel synthetic approach to fabricate NiCo LDHs was provided by Liang and co-workers by using a hydrothermal continuous-flow reactor (HCFR) at a high temperature (160 °C) under a high pressure of 160 psi.[71] The growth of NiCo LDHs can be easily scaled up onto conductive substrates, but also the morphology and structural features can be controlled *via* precursor supersaturation. The OER performance reached an overpotential of 367 mV for $J = 10$ mA cm^{-2} and a Tafel slope of 40 mV dec^{-1}. More interestingly, Jia *et al.*[102] synthesized a ternary CoNiMn-layered double hydroxides (LDH)/polypyrrole (PPy)/reduced graphene oxide (RGO) composite *via* coprecipitation of LDHs and simultaneous polymerization of the pyrrole (Py). As a result of the synergistic effect among the different components, the prepared CoNiMn-LDH/PPy/RGO exhibited excellent electrocatalytic activities for the OER and oxygen reduction reaction (ORR). In particular, a small overpotential of 369 mV was achieved at $J = 10$ mA cm^{-2} for the OER.

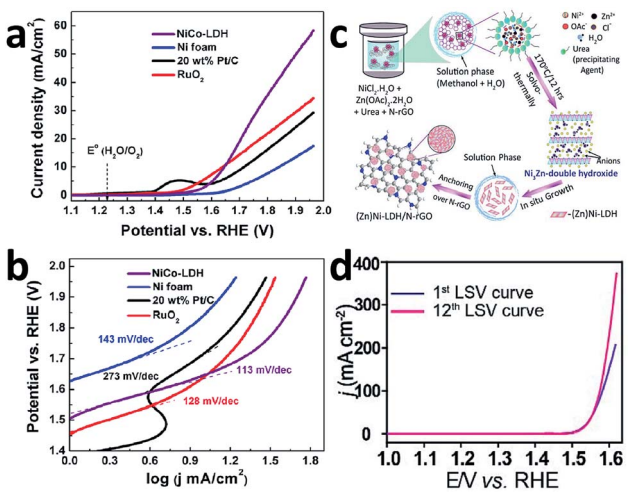

Fig. 17 (a) Polarization curves and (b) Tafel plot derived from the corresponding polarization curves. All the measurements were performed in O_2-saturated 0.1 M KOH solution (pH = 13 at a scan rate of 5 mV s^{-1}). Reproduced with permission from ref. 136. Copyright 2015, Elsevier B.V., (c) schematic illustration of solvothermal synthesis of (Zn) Ni-LDH/NRGO electrocatalysts and (d) polarization curves recorded at a scan rate of 10 mV s^{-1} with two different loop numbers. Reproduced with permission from ref. 153. Copyright 2017, The Royal Society of Chemistry.

3.4 Other LDHs

As already discussed above, large numbers of reports have concentrated on the design of LDHs by combining iron-group elements, *i.e.* Ni, Fe, or Co. Yet, the combination of iron-group elements with other transition metal elements is also of great interest. Fan *et al.* synthesized a monolayer of nickel vanadium layered double hydroxide (NiV LDH). A current density of 57 mA cm^{-2} was achieved after ohmic-drop correction at an overpotential of 350 mV for the OER.[141] Synthesis of NiMn LDH nanoplatelets was studied by Ma and co-workers[152] with a molar ratio of 2 : 1 in Ni^{2+}/Mn^{2+} salt precursors *via* hydrothermal treatment. After anion-exchange with dodecyl sulfate anions, the LDHs were exfoliated and subsequently flocculated with (reduced) graphene oxide (GO/RGO). The overpotential required at $J = 10$ mA cm^{-2} for NiMn LDH/RGO was 100 mV, smaller than that for NiMn LDH (360 mV).

Similarly, Nadeema and co-workers fabricated NiZn LDHs/nitrogen doped RGO *via* a solvothermal method (Fig. 17c). The incorporation of Zn^{2+} could facilitate the formation of high-oxidation-state Ni^{3+} and phase transformation of γ-NiOOH, promoting the OER smoothly at a low overpotential of 290 mV for $J = 10$ mA cm^{-2}. After the faradaic impedance measurements, the charge transfer resistance (R_{ct}) was decreased and accordingly the OER activity was increased along with the increasing loops of LSV (Fig. 17d).[153] Jia and co-workers prepared two types of multi-wall carbon nanotube (MWCNT) based CoMn LDH and NiMn LDH hybrids *via* a simple chemical bath deposition method. By control of the cation ratio, the Co_5Mn-LDH/MWCNT and Ni_5Mn-LDH/MWCNT are found to have the best OER activities, generating $J = 10$ mA cm^{-2} at overpotentials of 300 and 350 mV, respectively.[154] With respect to the thermodynamic impacts, the presence of excess manganese ions in the crystal structure increased the binding force

between Mn and O, resulting in the increase of the onset overpotential. It is necessary to reduce the amount of stable manganese ions and weaken the bond strength between Mn and O. On the other hand excess Co or Ni ions may lead to local structural deformation of the ordered graphite sheet and formation of $Co(OH)_2$ or $Ni(OH)_2$ aggregates.[154]

3.5 Relevant photochemical and photoelectrochemical applications

Apart from being used as the anode OER catalyst in electrochemical water splitting (Fig. 18a), the application of a couple of LDH OER catalysts in photochemical and photoelectrochemical water splitting systems was achieved for highly efficient solar energy conversion.[164] Recently, several kinds of LDHs have been intensively investigated, which played an important role in photochemical and photoelectrochemical water splitting.[165–168] Roger *et al.* proposed two schematics of photoelectrochemical solar-to-hydrogen artificial photosynthesis systems, *i.e.*, wireless and wired configurations (Fig. 18b and c). A buried photovoltaic layer is responsible for light harvesting (Fig. 18b) and a semiconductor photoelectrocatalyst film underneath each electrocatalyst (Fig. 18c). In both cases, light must pass through the catalysts as completely as possible. Therefore, thin layered LDH catalysts (near-transparent) can be one of the most promising candidates.

Hu *et al.* reported that by deposition of an optically transparent $FeNiO_x$ catalyst on nanostructured hematite photoanodes (Fig. 18d), the onset potential was shifted cathodically by 0.2 V (Fig. 18e).[168] Li *et al.* modified a $BiVO_4$ photoanode with a multi-functional CoAl LDH overlayer for PEC water oxidation (Fig. 18f).[165] Compared to pristine $BiVO_4$, the onset potential of CoAl LDH@$BiVO_4$ was greatly reduced from 0.90 V to 0.36 V (Fig. 18g). In light of the band engineering concept, there is an interesting demonstration that a series of Zn/Ti, Zn/Ce, and Zn/Cr LDHs can be used as "doped semiconducting" photocatalysts for extension of the optical absorption range into the visible light region and oxygen generation by solar water splitting.[169]

4 Conclusion and future perspectives

In this review, we discuss the key issues in designing LDH electrocatalysts as well as highlight the synthetic strategies. The recent advances in LDH electrocatalysts for the anodic half-reaction of the OER are summarized in detail. Although LDH materials have attracted wide attention because of their low cost and easy accessibility, there is still much room for performance improvements. A sophisticated understanding of the determining factors requires the following:

(i) It is crucial to precisely control the structure of LDHs, such as more uniformly aligned LDH nanoarrays, hierarchically porous LDH nanosheets, and ultrathin few-layer LDHs.

(ii) The support of LDHs needs to be further sought to optimize the conductivity, such as metal-based current collectors and supports with active sites like graphene-based materials.

(iii) The functional roles of the active sites in LDH materials is not entirely clear, but is only generalized using the synergistic

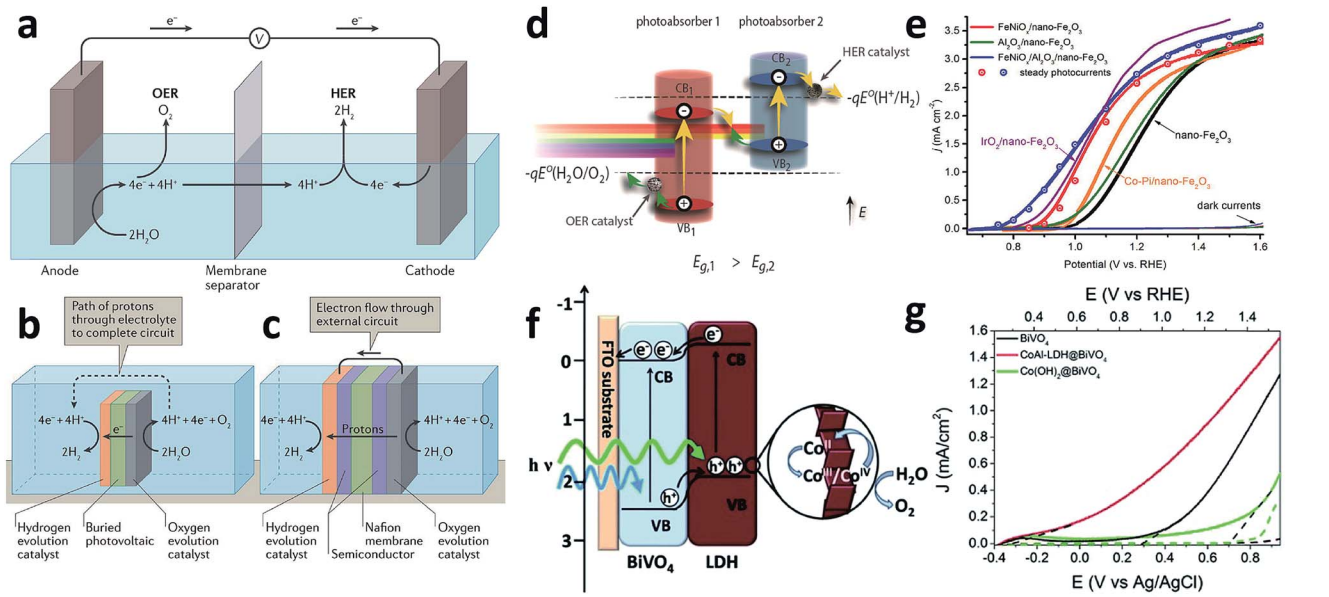

Fig. 18 (a) Archetypal electrolysis cell for water splitting, (b) wireless configuration in which proton flow through the electrolyte completes the circuit, and (c) wired configuration in which the electrical circuit is completed by external wiring. Reproduced with permission from ref. 164. Copyright 2018, Springer Nature Publishing AG, (d) schematic for a photoelectrochemical tandem cell. (e) CV curve of the OER under AM 1.5 illumination (1 sun) for nano-Fe_2O_3 photoanodes coated with different catalysts and ultrathin Al_2O_3. Reproduced with permission from ref. 168. Copyright 2015, American Chemical Society. (f) Schematic mechanism of LDH@$BiVO_4$ for PEC water oxidation, and (g) LSV curves of the photoanodes under 1 sun illumination (solid line) and in the dark (dashed line). Reproduced with permission from ref. 165. Copyright 2015, The Royal Society of Chemistry.

effect between the active sites. It is necessary to unambiguously clarify the possible origins of different types of active sites from both experimental and theoretical aspects, especially the appropriate ratio of different active sites to reduce he energy barrier of the rate-determining step during the OER.

(iv) Theoretical calculations of materials, especially using DFT + U method for transition metal element based materials, which can be helpful for estimating the adsorption and desorption capacity of the active site, band gap, free energy change of each catalytic step, *etc.*, and also providing support for researchers in screening high-performance LDH materials.

(v) The performance of most LDHs remains mainly dependent on alkaline conditions. However, it causes severe corrosions of electrodes and cell components for a long-term application run of at least 1000 h. It is highly desirable to elucidate the catalytic mechanism of LDH-based electrocatalysts for water splitting in neutral electrolyte solution at an atomistic and molecular level from both theoretical and experimental sides, especially, the revealing of dynamic behaviours.

(vi) The *in situ*/operando characterization techniques (*e.g.*, electrochemistry or microscopy/spectroscopy) are rising, which may aid efforts to understand fundamental aspects of the reaction transformation processes at the molecular level. In order to determine the real performance and stability of a catalyst, a standardized protocol needs to be developed, which can be further used to explore novel advanced materials and search for a potential catalyst for real devices.

With this comprehensive overview, as we believe, the readers are now enlightened with the current trends in designing and evaluating LDH based OER electrocatalysts for electrochemical applications. Also, this review enables the reader to get recent updates on the development of such LDH electrocatalysts, which could surely help them to work on the related high performance catalysts.

Conflicts of interest

There are no conflicts to declare.

Acknowledgements

We greatly appreciate the financial support from the National Natural Science Foundation of China (51572173, 51602197, 51771121 and 51702212), Shanghai Municipal Science and Technology Commission (16060502300, 16JC402200 and 18511110600), and Shanghai Eastern Scholar Program (QD2016014).

Notes and references

1 J. O. M. Bockris, *Int. J. Hydrogen Energy*, 2002, **27**, 731–740.
2 I. Dincer, *Int. J. Hydrogen Energy*, 2012, **37**, 1954–1971.
3 S. Chu and A. Majumdar, *Nature*, 2012, **488**, 294–303.
4 I. Dincer and C. Acar, *Int. J. Hydrogen Energy*, 2015, **40**, 11094–11111.
5 P. Parthasarathy and K. S. Narayanan, *Renewable Energy*, 2014, **66**, 570–579.
6 G. Wu, A. Santandreu, W. Kellogg, S. Gupta, O. Ogoke, H. Zhang, H.-L. Wang and L. Dai, *Nano Energy*, 2016, **29**, 83–110.
7 N. S. Lewis and D. G. Nocera, *Proc. Natl. Acad. Sci. U. S. A.*, 2006, **103**, 15729–15735.
8 Y. Jiao, Y. Zheng, M. Jaroniec and S. Z. Qiao, *Chem. Soc. Rev.*, 2015, **44**, 2060–2086.
9 M. W. Kanan and D. G. Nocera, *Science*, 2008, **321**, 1072–1075.
10 T. Audichon, T. W. Napporn, C. Canaff, C. Morais, C. Comminges and K. B. Kokoh, *J. Phys. Chem. C*, 2016, **120**, 2562–2573.
11 M. Carmo, D. L. Fritz, J. Merge and D. Stolten, *Int. J. Hydrogen Energy*, 2013, **38**, 4901–4934.
12 S. Cherevko, S. Geiger, O. Kasian, N. Kulyk, J.-P. Grote, A. Savan, B. R. Shrestha, S. Merzlikin, B. Breitbach, A. Ludwig and K. J. J. Mayrhofer, *Catal. Today*, 2016, **262**, 170–180.
13 Y. Lee, J. Suntivich, K. J. May, E. E. Perry and Y. Shao-Horn, *J. Phys. Chem. Lett.*, 2012, **3**, 399–404.
14 S. Park, D. Yoon, S. Bang, J. Kim, H. Baik, H. Yang and K. Lee, *Nanoscale*, 2015, **7**, 15065–15069.
15 R. R. Rao, M. J. Kolb, N. B. Halck, A. F. Pedersen, A. Mehta, H. You, K. A. Stoerzinger, Z. Feng, H. A. Hansen, H. Zhou, L. Giordano, J. Rossmeisl, T. Vegge, I. Chorkendorff, I. E. L. Stephens and Y. Shao-Horn, *Energy Environ. Sci.*, 2017, **10**, 2626–2637.
16 T. Reier, Z. Pawolek, S. Cherevko, M. Bruns, T. Jones, D. Teschner, S. Selve, A. Bergmann, H. N. Nong, R. Schloegl, K. J. J. Mayrhofer and P. Strasser, *J. Am. Chem. Soc.*, 2015, **137**, 13031–13040.
17 M. G. Walter, E. L. Warren, J. R. McKone, S. W. Boettcher, Q. Mi, E. A. Santori and N. S. Lewis, *Chem. Rev.*, 2011, **111**, 5815.
18 W. T. Hong, M. Risch, K. A. Stoerzinger, A. Grimaud, J. Suntivich and Y. Shao-Horn, *Energy Environ. Sci.*, 2015, **8**, 1404–1427.
19 E. Antolini, *ACS Catal.*, 2014, **4**, 1426–1440.
20 R. Kötz, H. J. Lewerenz and S. Stucki, *J. Electrochem. Soc.*, 1983, **130**, 825–829.
21 R. Kötz, H. Neff and S. Stucki, *J. Electrochem. Soc.*, 1984, **131**, 72–77.
22 M. Tahir, L. Pan, F. Idrees, X. Zhang, L. Wang, J.-J. Zou and Z. L. Wang, *Nano Energy*, 2017, **37**, 136–157.
23 S. Anantharaj, S. R. Ede, K. Sakthikumar, K. Karthick, S. Mishra and S. Kundu, *ACS Catal.*, 2016, **6**, 8069–8097.
24 A. Guzmán-Vargas, J. Vazquez-Samperio, M. A. Oliver-Tolentino, N. Nava, N. Castillo, M. J. Macías-Hernández and E. Reguera, *J. Mater. Sci.*, 2018, **53**, 4515–4526.
25 J. Wang, W. Cui, Q. Liu, Z. Xing, A. M. Asiri and X. Sun, *Adv. Mater.*, 2016, **28**, 215–230.
26 T. Zhan, X. Liu, S. Lu and W. Hou, *Appl. Catal., B*, 2017, **205**, 551–558.
27 M. Al-Mamun, X. Su, H. Zhang, H. Yin, P. Liu, H. Yang, D. Wang, Z. Tang, Y. Wang and H. Zhao, *Small*, 2016, **12**, 2866–2871.

28 Z. Chen, C. X. Kronawitter and B. E. Koel, *Phys. Chem. Chem. Phys.*, 2015, **17**, 29387–29393.
29 S. Hirai, S. Yagi, A. Seno, M. Fujioka, T. Ohno and T. Matsuda, *RSC Adv.*, 2016, **6**, 2019–2023.
30 M. Li, Y. Xiong, X. Liu, X. Bo, Y. Zhang, C. Han and L. Guo, *Nanoscale*, 2015, **7**, 8920–8930.
31 Y. Matsumoto, S. Yamada, T. Nishida and E. Sato, *J. Electrochem. Soc.*, 1980, **127**, 2360–2364.
32 J. O. M. Bockris and T. Otagawa, *J. Electrochem. Soc.*, 1984, **131**, 290–302.
33 R. D. L. Smith, M. S. Prevot, R. D. Fagan, S. Trudel and C. P. Berlinguette, *J. Am. Chem. Soc.*, 2013, **135**, 11580–11586.
34 S. Yagi, I. Yamada, H. Tsukasaki, A. Seno, M. Murakami, H. Fujii, H. Chen, N. Umezawa, H. Abe, N. Nishiyama and S. Mori, *Nat. Commun.*, 2015, **6**, 8249.
35 Y. Zhu, W. Zhou, J. Yu, Y. Chen, M. Liu and Z. Shao, *Chem. Mater.*, 2016, **28**, 1691–1697.
36 D. Li, H. Baydoun, C. N. Verani and S. L. Brock, *J. Am. Chem. Soc.*, 2016, **138**, 4006–4009.
37 L.-A. Stern, L. Feng, F. Song and X. Hu, *Energy Environ. Sci.*, 2015, **8**, 2347–2351.
38 J. Xing, H. Li, M. M.-C. Cheng, S. M. Geyer and K. Y. S. Ng, *J. Mater. Chem. A*, 2016, **4**, 13866–13873.
39 A. T. Swesi, J. Masud and M. Nath, *Energy Environ. Sci.*, 2016, **9**, 1771–1782.
40 C. Xia, Q. Jiang, C. Zhao, M. N. Hedhili and H. N. Alshareef, *Adv. Mater.*, 2016, **28**, 77–85.
41 X. Xu, F. Song and X. Hu, *Nat. Commun.*, 2016, **7**, 12324.
42 P. Cai, J. Huang, J. Chen and Z. Wen, *Angew. Chem., Int. Ed.*, 2017, **56**, 4858–4861.
43 B. Dong, X. Zhao, G. Q. Han, X. Li, X. Shang, Y.-R. Liu, W.-H. Hu, Y.-M. Chai, H. Zhao and C. G. Liu, *J. Mater. Chem. A*, 2016, **4**, 13499–13508.
44 T. Liu, Y. Liang, Q. Liu, X. Sun, Y. He and A. M. Asiri, *Electrochem. Commun.*, 2015, **60**, 92–96.
45 P. Chen, K. Xu, Z. Fang, Y. Tong, J. Wu, X. Lu, X. Peng, H. Ding, C. Wu and Y. Xie, *Angew. Chem., Int. Ed.*, 2015, **54**, 14710–14714.
46 P. Chen, K. Xu, Y. Tong, X. Li, S. Tao, Z. Fang, W. Chu, X. Wu and C. Wu, *Inorg. Chem. Front.*, 2016, **3**, 236–242.
47 M. Shalom, D. Ressnig, X. Yang, G. Clavel, T. P. Fellinger and M. Antonietti, *J. Mater. Chem. A*, 2015, **3**, 8171–8177.
48 Y. Zhang, B. Ouyang, J. Xu, G. Jia, S. Chen, R. S. Rawat and H. J. Fan, *Angew. Chem., Int. Ed.*, 2016, **55**, 8670–8674.
49 L. Cui, F. Qu, J. Liu, G. Du, A. M. Asiri and X. Sun, *ChemSusChem*, 2017, **10**, 1370–1374.
50 J. Masa, I. Sinev, H. Mistry, E. Ventosa, M. de la Mata, J. Arbiol, M. Muhler, B. Roldan Cuenya and W. Schuhmann, *Adv. Energy Mater.*, 2017, **7**, 1700381.
51 J. Masa, P. Weide, D. Peeters, I. Sinev, W. Xia, Z. Sun, C. Somsen, M. Muhler and W. Schuhmann, *Adv. Energy Mater.*, 2016, **6**, 1502313.
52 J. Jiang, Q. Liu, C. Zeng and L. Ai, *J. Mater. Chem. A*, 2017, **5**, 16929–16935.
53 J. Su, G. Xia, R. Li, Y. Yang, J. Chen, R. Shi, P. Jiang and Q. Chen, *J. Mater. Chem. A*, 2016, **4**, 9204–9212.
54 H. Wang, Y. Cao, C. Sun, G. Zou, J. Huang, X. Kuai, J. Zhao and L. Gao, *ChemSusChem*, 2017, **10**, 3540–3546.
55 S. W. Sheehan, J. M. Thomsen, U. Hintermair, R. H. Crabtree, G. W. Brudvig and C. A. Schmuttenmaer, *Nat. Commun.*, 2015, **6**, 6469.
56 B. Wurster, D. Grumelli, D. Hoetger, R. Gutzler and K. Kern, *J. Am. Chem. Soc.*, 2016, **138**, 3623–3626.
57 M. Gong, Y. Li, H. Wang, Y. Liang, J. Z. Wu, J. Zhou, J. Wang, T. Regier, F. Wei and H. Dai, *J. Am. Chem. Soc.*, 2013, **135**, 8452–8455.
58 C. Li, M. Wei, D. G. Evans and X. Duan, *Small*, 2014, **10**, 4469–4486.
59 C. Tang, H. F. Wang, X.-L. Zhu, B. Q. Li and Q. Zhang, *Part. Part. Syst. Charact.*, 2016, **33**, 473–486.
60 F. Song, L. Bai, A. Moysiadou, S. Lee, C. Hu, L. Liardet and X. Hu, *J. Am. Chem. Soc.*, 2018, **140**, 7748–7759.
61 Z. Gu, J. J. Atherton and Z. P. Xu, *Chem. Commun.*, 2015, **51**, 3024–3036.
62 Y. Zhao, B. Li, Q. Wang, W. Gao, C. J. Wang, M. Wei, D. G. Evans, X. Duan and D. O'Hare, *Chem. Sci.*, 2014, **5**, 951–958.
63 S. Liu, S. C. Lee, U. Patil, I. Shackery, S. Kang, K. Zhang, J. H. Park, K. Y. Chung and S. C. Jun, *J. Mater. Chem. A*, 2017, **5**, 1043–1049.
64 Q. Wang, L. Shang, R. Shi, X. Zhang, Y. Zhao, G. I. N. Waterhouse, L.-Z. Wu, C.-H. Tung and T. Zhang, *Adv. Energy Mater.*, 2017, **7**, 1700467.
65 L. N. M. Ribeiro, A. C. S. Alcantara, M. Darder, P. Aranda, F. M. Araujo-Moreira and E. Ruiz-Hitzky, *Int. J. Pharm.*, 2014, **463**, 1–9.
66 G. Fan, F. Li, D. G. Evans and X. Duan, *Chem. Soc. Rev.*, 2014, **43**, 7040–7066.
67 Q. Wang and D. O'Hare, *Chem. Rev.*, 2012, **112**, 4124–4155.
68 S.-M. Xu, T. Pan, Y.-B. Dou, H. Yan, S.-T. Zhang, F.-Y. Ning, W.-Y. Shi and M. Wei, *J. Phys. Chem. C*, 2015, **119**, 18823–18834.
69 M. Gong and H. Dai, *Nano Res.*, 2015, **8**, 23–39.
70 H. Liang, L. Li, F. Meng, L. Dang, J. Zhuo, A. Forticaux, Z. Wang and S. Jin, *Chem. Mater.*, 2015, **27**, 5702–5711.
71 H. Liang, F. Meng, M. Caban-Acevedo, L. Li, A. Forticaux, L. Xiu, Z. Wang and S. Jin, *Nano Lett.*, 2015, **15**, 1421–1427.
72 A. Sengeni, K. Karthick and S. Kundu, *Mater. Today Energy*, 2017, **6**, 1–26.
73 G. B. B. Varadwaj and V. Nyamori, *Nano Res.*, 2016, **9**, 3598–3621.
74 L. Zhou, M. Shao, M. Wei and X. Duan, *J. Energy Chem.*, 2017, **26**, 1094–1106.
75 H. Dau, C. Limberg, T. Reier, M. Risch, S. Roggan and P. Strasser, *ChemCatChem*, 2010, **2**, 724–761.
76 P. Li, X. Duan, Y. Kuang, Y. Li, G. Zhang, W. Liu and X. Sun, *Adv. Energy Mater.*, 2018, **8**, 1703341.
77 F. S. Zhang, J.-W. Wang, J. Luo, R. R. Liu, Z.-M. Zhang, C. T. He and T. B. Lu, *Chem. Sci.*, 2018, **9**, 1375–1384.
78 D. Zhou, Z. Cai, Y. Bi, W. Tian, M. Luo, Q. Zhang, Q. Xie, J. Wang, Y. Li, Y. Kuang, X. Duan, M. Bajdich, S. Siahrostami and X. Sun, *Nano Res.*, 2018, **11**, 1358–1368.

79 W. Zhu, Z. Yue, W. Zhang, N. Hu, Z. Luo, M. Ren, Z. Xu, Z. Wei, Y. Suo and J. Wang, *J. Mater. Chem. A*, 2018, **6**, 4346–4353.
80 C. C. L. McCrory, S. Jung, J. C. Peters and T. F. Jaramillo, *J. Am. Chem. Soc.*, 2013, **135**, 16977–16987.
81 F. Dionigi and P. Strasser, *Adv. Energy Mater.*, 2016, **6**, 1600621.
82 E. Fabbri, A. Habereder, K. Waltar, R. Koetz and T. J. Schmidt, *Catal. Sci. Technol.*, 2014, **4**, 3800–3821.
83 C. Yu, Z. Liu, X. Han, H. Huang, C. Zhao, J. Yang and J. Qiu, *Carbon*, 2016, **110**, 1–7.
84 J. Garche, C. K. Dyer, P. T. Moseley, Z. Ogumi, D. A. Rand and B. Scrosati, *Encyclopedia of Electrochemical Power Sources*, Newnes, 2013.
85 D. Rand and R. M. Dell, *Hydrogen Energy: Challenges and Prospects*, Royal Society of Chemistry, 2007.
86 K. Zeng and D. Zhang, *Prog. Energy Combust. Sci.*, 2010, **36**, 307–326.
87 L. M. Gandía, G. Arzamendi and P. M. Diéguez, *Renewable Hydrogen Energy: an Overview*, Elsevier, Amsterdam, 2013, ch. 1.
88 K. Rajeshwar, R. McConnell and S. Licht, *Solar Hydrogen Generation: toward a Renewable Energy Future*, Springer, 2008.
89 J. Ji, L. L. Zhang, H. Ji, Y. Li, X. Zhao, X. Bai, X. Fan, F. Zhang and R. S. Ruoff, *ACS Nano*, 2013, **7**, 6237–6243.
90 X. G. Liu, X. Wang, X. T. Yuan, W. J. Dong and F. Q. Huang, *J. Mater. Chem. A*, 2016, **4**, 167–172.
91 F. Song and X. Hu, *Nat. Commun.*, 2014, **5**, 4477.
92 S. Anantharaj, K. Karthick, M. Venkatesh, T. V. S. V. Simha, A. S. Salunke, L. Ma, H. Liang and S. Kundu, *Nano Energy*, 2017, **39**, 30–43.
93 X. Han, C. Yu, J. Yang, C. Zhao, H. Huang, Z. Liu, P. M. Ajayan and J. Qiu, *Adv. Mater. Interfaces*, 2016, **3**, 1500782.
94 Y. Shao, M. Zheng, M. Cai, L. He and C. Xu, *Electrochim. Acta*, 2017, **257**, 1–8.
95 C. Zhang, M. Shao, L. Zhou, Z. Li, K. Xiao and M. Wei, *ACS Appl. Mater. Interfaces*, 2016, **8**, 33697–33703.
96 X. Lu and C. Zhao, *Nat. Commun.*, 2015, **6**, 6616.
97 J. Huang, J. Chen, T. Yao, J. He, S. Jiang, Z. Sun, Q. Liu, W. Cheng, F. Hu, Y. Jiang, Z. Pan and S. Wei, *Angew. Chem., Int. Ed.*, 2015, **54**, 8722–8727.
98 H. Vrubel, T. Moehl, M. Graetzel and X. Hu, *Chem. Commun.*, 2013, **49**, 8985–8987.
99 Z. Lu, W. Xu, W. Zhu, Q. Yang, X. Lei, J. Liu, Y. Li, X. Sun and X. Duan, *Chem. Commun.*, 2014, **50**, 6479–6482.
100 H. Liu, Y. Wang, X. Lu, Y. Hu, G. Zhu, R. Chen, L. Ma, H. Zhu, Z. Tie, J. Liu and Z. Jin, *Nano Energy*, 2017, **35**, 350–357.
101 Z. Lu, L. Qian, Y. Tian, Y. Li, X. Sun and X. Duan, *Chem. Commun.*, 2016, **52**, 908–911.
102 X. Jia, S. Gao, T. Liu, D. Li, P. Tang and Y. Feng, *Electrochim. Acta*, 2017, **245**, 51–60.
103 L. Qian, Z. Lu, T. Xu, X. Wu, Y. Tian, Y. Li, Z. Huo, X. Sun and X. Duan, *Adv. Energy Mater.*, 2015, **5**, 1500245.
104 A.-L. Wang, H. Xu and G.-R. Li, *ACS Energy Lett.*, 2016, **1**, 445–453.
105 A. Bergmann, E. Martinez-Moreno, D. Teschner, P. Chernev, M. Gliech, J. F. de Araujo, T. Reier, H. Dau and P. Strasser, *Nat. Commun.*, 2015, **6**, 8625.
106 K. Xu, P. Z. Chen, X. L. Li, Y. Tong, H. Ding, X. J. Wu, W. S. Chu, Z. M. Peng, C. Z. Wu and Y. Xie, *J. Am. Chem. Soc.*, 2015, **137**, 4119–4125.
107 J. Ping, Y. Wang, Q. Lu, B. Chen, J. Chen, Y. Huang, Q. Ma, C. Tan, J. Yang, X. Cao, Z. Wang, J. Wu, Y. Ying and H. Zhang, *Adv. Mater.*, 2016, **28**, 7640–7645.
108 X. Long, J. Li, S. Xiao, K. Yan, Z. Wang, H. Chen and S. Yang, *Angew. Chem., Int. Ed.*, 2014, **53**, 7584–7588.
109 B. M. Hunter, W. Hieringer, J. R. Winkler, H. B. Gray and A. M. Mueller, *Energy Environ. Sci.*, 2016, **9**, 1734–1743.
110 L. Zhuang, L. Ge, Y. Yang, M. Li, Y. Jia, X. Yao and Z. Zhu, *Adv. Mater.*, 2017, **29**, 1606793.
111 Y. Sun, S. Gao, F. Lei and Y. Xie, *Chem. Soc. Rev.*, 2015, **44**, 623–636.
112 Y. Wang, Y. Zhang, Z. Liu, C. Xie, S. Feng, D. Liu, M. Shao and S. Wang, *Angew. Chem., Int. Ed.*, 2017, **56**, 5867–5871.
113 M. Asnavandi, Y. Yin, Y. Li, C. Sun and C. Zhao, *ACS Energy Lett.*, 2018, **3**, 1515–1520.
114 R. Liu, Y. Wang, D. Liu, Y. Zou and S. Wang, *Adv. Mater.*, 2017, **29**, 1701546.
115 Y. Wang, M. Qiao, Y. Li and S. Wang, *Small*, 2018, **14**, 1800136.
116 M.-Q. Yang, J. Wang, H. Wu and G. W. Ho, *Small*, 2018, **14**, 1703323.
117 Y. Zhao, X. Zhang, X. Jia, G. I. N. Waterhouse, R. Shi, X. Zhang, F. Zhan, Y. Tao, L.-Z. Wu, C.-H. Tung, D. O'Hare and T. Zhang, *Adv. Energy Mater.*, 2018, **8**, 1703585.
118 D. Zhou, X. Xiong, Z. Cai, N. Han, Y. Jia, Q. Xie, X. Duan, T. Xie, X. Zheng, X. Sun and X. Duan, *Small Methods*, 2018, **2**, 1800083.
119 P. Zhou, Y. Wang, C. Xie, C. Chen, H. Liu, R. Chen, J. Huo and S. Wang, *Chem. Commun.*, 2017, **53**, 11778–11781.
120 Y. Zhao, X. Jia, G. Chen, L. Shang, G. I. N. Waterhouse, L.-Z. Wu, C.-H. Tung, D. O'Hare and T. Zhang, *J. Am. Chem. Soc.*, 2016, **138**, 6517–6524.
121 W. Cheng, H. Zhang, X. Zhao, H. Su, F. Tang, J. Tian and Q. Liu, *J. Mater. Chem. A*, 2018, **6**, 9420–9427.
122 M. S. Burke, S. Zou, L. J. Enman, J. E. Kellon, C. A. Gabor, E. Pledger and S. W. Boettcher, *J. Phys. Chem. Lett.*, 2015, **6**, 3737–3742.
123 A. M. Smith, L. Trotochaud, M. S. Burke and S. W. Boettcher, *Chem. Commun.*, 2015, **51**, 5261–5263.
124 L. Trotochaud, J. K. Ranney, K. N. Williams and S. W. Boettcher, *J. Am. Chem. Soc.*, 2012, **134**, 17253–17261.
125 L. Trotochaud, S. L. Young, J. K. Ranney and S. W. Boettcher, *J. Am. Chem. Soc.*, 2014, **136**, 6744–6753.
126 S. Zou, M. S. Burke, M. G. Kast, J. Fan, N. Danilovic and S. W. Boettcher, *Chem. Mater.*, 2015, **27**, 8011–8020.
127 M. S. Burke, M. G. Kast, L. Trotochaud, A. M. Smith and S. W. Boettcher, *J. Am. Chem. Soc.*, 2015, **137**, 3638–3648.
128 D. Friebel, M. W. Louie, M. Bajdich, K. E. Sanwald, Y. Cai, A. M. Wise, M.-J. Cheng, D. Sokaras, T.-C. Weng, R. Alonso-Mori, R. C. Davis, J. R. Bargar, J. K. Nørskov, A. Nilsson and A. T. Bell, *J. Am. Chem. Soc.*, 2015, **137**, 1305–1313.

129 J. Zhang, J. Liu, L. Xi, Y. Yu, N. Chen, S. Sun, W. Wang, K. M. Lange and B. Zhang, *J. Am. Chem. Soc.*, 2018, **140**, 3876–3879.
130 J. Y. C. Chen, L. Dang, H. Liang, W. Bi, J. B. Gerken, S. Jin, E. E. Alp and S. S. Stahl, *J. Am. Chem. Soc.*, 2015, **137**, 15090–15093.
131 J. Suntivich, K. J. May, H. A. Gasteiger, J. B. Goodenough and Y. Shao-Horn, *Science*, 2011, **334**, 1383–1385.
132 Q. Dong, Q. Wang, Z. Dai, H. Qiu and X. Dong, *ACS Appl. Mater. Interfaces*, 2016, **8**, 26902–26907.
133 Y. Liu, H. Cheng, M. Lyu, S. Fan, Q. Liu, W. Zhang, Y. Zhi, C. Wang, C. Xiao, S. Wei, B. Ye and Y. Xie, *J. Am. Chem. Soc.*, 2014, **136**, 15670–15675.
134 M. Bajdich, M. Garcia-Mota, A. Vojvodic, J. K. Norskov and A. T. Bell, *J. Am. Chem. Soc.*, 2013, **135**, 13521–13530.
135 L. Yu, H. Zhou, J. Sun, F. Qin, D. Luo, L. Xie, F. Yu, J. Bao, Y. Li, Y. Yu, S. Chen and Z. Ren, *Nano Energy*, 2017, **41**, 327–336.
136 J. Jiang, A. Zhang, L. Li and L. Ai, *J. Power Sources*, 2015, **278**, 445–451.
137 J. Li, W. Xu, R. Li, J. Luo, D. Zhou, S. Li, P. Cheng and D. Yuan, *J. Mater. Sci.*, 2016, **51**, 9287–9295.
138 J. Wu, Z. Ren, S. Du, L. Kong, B. Liu, W. Xi, J. Zhu and H. Fu, *Nano Res.*, 2016, **9**, 713–725.
139 K. Fominykh, P. Chernev, I. Zaharieva, J. Sicklinger, G. Stefanic, M. Doeblinger, A. Mueller, A. Pokharel, S. Boecklein, C. Scheu, T. Bein and D. Fattakhova-Rohlfing, *ACS Nano*, 2015, **9**, 5180–5188.
140 H. Wang, H.-W. Lee, Y. Deng, Z. Lu, P.-C. Hsu, Y. Liu, D. Lin and Y. Cui, *Nat. Commun.*, 2015, **6**, 7261.
141 K. Fan, H. Chen, Y. Ji, H. Huang, P. M. Claesson, Q. Daniel, B. Philippe, H. Rensmo, F. Li, Y. Luo and L. Sun, *Nat. Commun.*, 2016, **7**, 11981.
142 Y. Jia, L. Zhang, G. Gao, H. Chen, B. Wang, J. Zhou, M. T. Soo, M. Hong, X. Yan, G. Qian, J. Zou, A. Du and X. Yao, *Adv. Mater.*, 2017, **29**, 1700017.
143 D. H. Youn, Y. Bin Park, J. Y. Kim, G. Magesh, Y. J. Jang and J. S. Lee, *J. Power Sources*, 2015, **294**, 437–443.
144 Y. Hou, M. R. Lohe, J. Zhang, S. Liu, X. Zhuang and X. Feng, *Energy Environ. Sci.*, 2016, **9**, 478–483.
145 D. Zhao, K. Jiang, Y. Pi and X. Huang, *ChemCatChem*, 2017, **9**, 84–88.
146 D. Tang, J. Liu, X. Wu, R. Liu, X. Han, Y. Han, H. Huang, Y. Liu and Z. Kang, *ACS Appl. Mater. Interfaces*, 2014, **6**, 7918–7925.
147 J. Yu, G. Cheng and W. Luo, *J. Mater. Chem. A*, 2017, **5**, 11229–11235.
148 Y. Jin, S. Huang, X. Yue, H. Du and P. K. Shen, *ACS Catal.*, 2018, **8**, 2359–2363.
149 L. Yu, H. Zhou, J. Sun, F. Qin, F. Yu, J. Bao, Y. Yu, S. Chen and Z. Ren, *Energy Environ. Sci.*, 2017, **10**, 1820–1827.
150 W. Zhu, L. Liu, Z. Yue, W. Zhang, X. Yue, J. Wang, S. Yu, L. Wang and J. Wang, *ACS Appl. Mater. Interfaces*, 2017, **9**, 19807–19814.
151 G. Chen, T. Wang, J. Zhang, P. Liu, H. Sun, X. Zhuang, M. Chen and X. Feng, *Adv. Mater.*, 2018, **30**, 1706279.
152 W. Ma, R. Ma, J. Wu, P. Sun, X. Liu, K. Zhou and T. Sasaki, *Nanoscale*, 2016, **8**, 10425–10432.
153 A. Nadeema, V. M. Dhavale and S. Kurungot, *Nanoscale*, 2017, **9**, 12590–12600.
154 G. Jia, Y. Hu, Q. Qian, Y. Yao, S. Zhang, Z. Li and Z. Zou, *ACS Appl. Mater. Interfaces*, 2016, **8**, 14527–14534.
155 F. Song and X. Hu, *J. Am. Chem. Soc.*, 2014, **136**, 16481–16484.
156 Y. Li, L. Zhang, X. Xiang, D. Yan and F. Li, *J. Mater. Chem. A*, 2014, **2**, 13250–13258.
157 J. Qi, W. Zhang, R. Xiang, K. Liu, H.-Y. Wang, M. Chen, Y. Han and R. Cao, *Adv. Sci.*, 2015, **2**, 1500199.
158 W. Zhang, J. Qi, K. Liu and R. Cao, *Adv. Energy Mater.*, 2016, **6**, 1502489.
159 R. Subbaraman, D. Tripkovic, K.-C. Chang, D. Strmcnik, A. P. Paulikas, P. Hirunsit, M. Chan, J. Greeley, V. Stamenkovic and N. M. Markovic, *Nat. Mater.*, 2012, **11**, 550–557.
160 Y. Jia, L. Zhang, A. Du, G. Gao, J. Chen, X. Yan, C. L. Brown and X. Yao, *Adv. Mater.*, 2016, **28**, 9532–9538.
161 X. Liu, J. Liu, Y. Li, Y. Li and X. Sun, *ChemCatChem*, 2014, **6**, 2501–2506.
162 Z. W. Seh, J. Kibsgaard, C. F. Dickens, I. B. Chorkendorff, J. K. Norskov and T. F. Jaramillo, *Science*, 2017, **355**, eaad4998.
163 H. Jin, J. Wang, D. Su, Z. Wei, Z. Pang and Y. Wang, *J. Am. Chem. Soc.*, 2015, **137**, 2688–2694.
164 I. Roger, M. A. Shipman and M. D. Symes, *Nat. Rev. Chem.*, 2017, **1**, 0003.
165 W. He, R. Wang, L. Zhang, J. Zhu, X. Xiang and F. Li, *J. Mater. Chem. A*, 2015, **3**, 17977–17982.
166 Y. Hou, Z. Wen, S. Cui, X. Feng and J. Chen, *Nano Lett.*, 2016, **16**, 2268–2277.
167 S. J. Kim, Y. Lee, D. K. Lee, J. W. Lee and J. K. Kang, *J. Mater. Chem. A*, 2014, **2**, 4136–4139.
168 C. G. Morales-Guio, M. T. Mayer, A. Yella, S. D. Tilley, M. Grätzel and X. Hu, *J. Am. Chem. Soc.*, 2015, **137**, 9927–9936.
169 C. G. Silva, Y. Bouizi, V. Fornés and H. García, *J. Am. Chem. Soc.*, 2009, **131**, 13833–13839.